Representation of Topography by Shaved Cells in a Height Coordinate Ocean Model

Alistair Adcroft, Chris Hill, and John Marshall

Department of Earth, Atmospheric and Planetary Sciences, Massachusetts Institute of Technology, Cambridge, Massachusetts

(Manuscript received 2 July 1996, in final form 13 December 1996)

ABSTRACT

Height coordinate ocean models commonly represent topography as a "staircase" of discontinuous steps that are fitted to the model grid. Here the ramifications of an alternative approach are studied in which "shaved cells" are used to represent irregular topography. The problem is formulated using the finite-volume method and care is taken to ensure that the discrete forms have appropriate conservation properties. Two representations of topography, "partial step" and "piecewise linear," are considered and compared with the staircase approach in some standard problems such as the topographic β effect and flow over a Gaussian bump. It is shown that shaved cells are clearly more accurate than the conventional staircase representation. The use of partial steps, although not as accurate as the piecewise linear approach, is seen to be superior to the staircase approach. Moreover, partial steps can be readily implemented in existing height coordinate models.

1. Introduction

Variations in the bottom relief of the atmosphere are typically a fraction of the depth of the troposphere and yet still influence the atmospheric circulation. Variations in the depth of the ocean are of order 1 and hence have a major control on the circulation. The accurate inclusion of topography in ocean models is therefore a major consideration. Topography is most commonly represented in height coordinate ocean models as "staircase" or "step" topography [used since Bryan (1969)], where the steps are chosen to fit the model grid (see Fig. 1a). As will be demonstrated later, this is a very crude approach that strictly only becomes reasonable in the limit of very high vertical and horizontal resolution.

Terrain-following coordinates can be used to represent topography (Fig. 1b) and clearly recognize the importance of the steering effect of topography on the ocean circulation (see Haidvogel et al. 1991; Blumberg and Mellor 1987). However, such models suffer from problems of "hydrostatic consistency," which can be particularly troublesome above steep slopes (see Haney 1991; Mellor et al. 1994). Height coordinates, on the other hand, recognize the overwhelming importance of gravity in the open ocean (the pressure surfaces are *almost* horizontal), but the crude "staircase" representation of topography leads to large errors.

The intent of this paper is to offer an alternative representation for use in height coordinate models in which we "shave" model cells to fit the ocean's topography (see Fig. 1c). This is the opposite philosophy of the "step topography" method in which the topography is fitted to the model grid. The "shaved cell" approach offers, we believe, many of the advantages of both height and terrain-following coordinates. We are able to show that the "shaved cell" method is potentially far superior to the "stepwise" representation in height coordinate models and can approach the fidelity of terrain-following coordinates without any of the hydrostatic consistency problems of the latter.

In order to introduce the discretization that allows the shaving of model cells, we first describe the "finite volume" technique. For a comprehensive introduction to the finite-volume method, we recommend Hirsch (1990). This discretization method is very similar to, but not the same as, the finite-differencing technique; in the interior of the ocean, the finite-volume and flux-form finite-difference discretizations are equivalent. The advantage of the finite volume approach in representing topography, however, is that the model cells need not be regular boxes and can thus be shaped to fit to the topography.

The paper is presented in three sections. Section 2 deals with the finite-volume formulation in general and applies it to the continuity and tracer conservation equations. In section 3 we discuss some possible representations of topography within the finite-volume formulation. We illustrate the clear advantages of "shaved cells" over "step" topography when applied to a two-dimensional passive tracer problem. The incompressible Boussinesq equations are then considered in section 4 and we present experiments of oceanographic interest (using the numerical model of Marshall et al.

Corresponding author address: Dr. Alistair Adcroft, Department of Earth, Atmospheric and Planetary Sciences, Massachusetts Institute of Technology, Cambridge, MA 02139.
E-mail: adcroft@plume.mit.edu

a) Step topography   b) σ-coordinates   c) Shaved cell
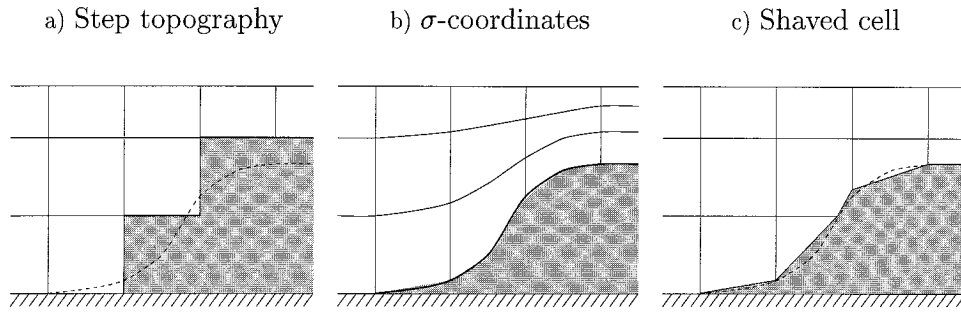
FIG. 1. The representation of a smoothly varying bottom (dashed line) in (a) a height coordinate model using step topography, (b) a terrain-following coordinate model, and (c) a height coordinate model with piecewise constant slopes.

1997a and 1997b), which demonstrate the applicability of the "shaved cell" method to more general problems involving topography.

2. The finite-volume method

Conservation of a scalar quantity ϕ, with sources Q, may be written in the general form:

$$\frac{\partial}{\partial t}\phi + \nabla \cdot \mathbf{F} = Q, \qquad (1)$$

where $\mathbf{F}$ is the vector flux of the quantity ϕ. Equation (1), when integrated over a constant[1] volume $\mathcal{V}$ enclosed by the surface $\mathcal{A}$, takes the form

$$\frac{\partial}{\partial t}\int_{\mathcal{V}}\phi\, d\mathcal{V} + \oint_{\mathcal{A}}\mathbf{F}\cdot d\mathcal{A} = \int_{\mathcal{V}} Q\, d\mathcal{V}, \qquad (2)$$

where we have made use of the Gauss divergence theorem, $d\mathcal{A} = d\mathcal{A}\mathbf{n}$ is an element of surface area, and $\mathbf{n}$ is a vector pointing along the outward normal of the surface $\mathcal{A}$. Thus, the variation of ϕ inside the volume depends only on the normal flux through the surface that defines the volume and the source terms within it. Equation (2) can be applied to a discrete control volume $\mathcal{V}_I$,

$$\mathcal{V}_I\frac{\partial}{\partial t}\phi_I + \sum_J F_{I,J}\mathcal{A}_{I,J} = \mathcal{V}_I Q_I, \qquad (3)$$

where the sum of the flux-area scalar products refers to all the external sides J of the control volume. The discrete variables are consistently defined by associating each term in (3) with its counterpart in (2):

---

[1] We limit the discussion here to control volumes that vary only in space. The method can be applied to temporally varying volumes, thereby allowing the use of both adaptive grids and other coordinate systems such as isentropic coordinates.

$$\mathcal{V}_I\frac{\partial}{\partial t}\phi_I = \frac{\partial}{\partial t}\int_{\mathcal{V}_I}\phi\, d\mathcal{V} \Rightarrow \phi_I \equiv \frac{1}{\mathcal{V}_I}\int_{\mathcal{V}_I}\phi\, d\mathcal{V}$$

$$F_{I,J}\mathcal{A}_{I,J} = \int_{\mathcal{A}_{I,J}}\mathbf{F}\cdot d\mathcal{A} \Rightarrow F_{I,J} \equiv \frac{1}{\mathcal{A}_{I,J}}\int_{\mathcal{A}_{I,J}}\mathbf{F}\cdot d\mathcal{A}$$

$$\mathcal{V}_I Q_I = \int_{\mathcal{V}_I} Q\, d\mathcal{V} \Rightarrow Q_I \equiv \frac{1}{\mathcal{V}_I}\int_{\mathcal{V}_I} Q\, d\mathcal{V}. \qquad (4)$$

That is, ϕ_I is the volume mean of ϕ within the control volume $\mathcal{V}_I$ and similarly for Q_I. Term $F_{I,J}$ is the area mean of the component of $\mathbf{F}$ normal to the side $\mathcal{A}_{I,J}$.

By adopting the definitions in (4), (3) is an exact statement. However, more often than not, $\mathbf{F}$ and Q are functions of the flow and must be found by interpolation. For example, suppose $\mathbf{F}$ is an advective flux $\mathbf{F} = \mathbf{v}\phi$ where $\mathbf{v}$ is specified. The surface integral of $\mathbf{F}$ becomes

$$\int_{\mathcal{A}_{I,J}}\mathbf{v}\phi\cdot d\mathcal{A} = \frac{1}{\mathcal{A}_{I,J}}\int_{\mathcal{A}_{I,J}}\mathbf{v}\cdot d\mathcal{A}\int_{\mathcal{A}_{I,J}}\phi\, d\mathcal{A} + \text{SGS}, \qquad (5)$$

where SGS represents terms resulting from the correlation of subgrid-scale variations of ϕ with $\mathbf{v}$ and will be set to zero here. If $\mathbf{v}$ is known on the face, the integral $\int \mathbf{v}\cdot d\mathcal{A}$ can be evaluated. The area mean of ϕ, however, must be approximated by interpolation of the volume-mean quantities ϕ_I to the face. This is the major source of truncation error in the discrete system

$$\frac{1}{\mathcal{A}_{I,J}}\int_{\mathcal{A}_{I,J}}\phi\, d\mathcal{A} \approx \overline{\phi_I}^J + O(\Delta_J^2\phi''), \qquad (6)$$

where $\overline{\phi_I}^J$ indicates interpolation of the volume-mean quantities to the face.

The control volumes must satisfy the following constraints for the system to be consistently conservative.

1) The sum of the control volumes $\mathcal{V}_I$ must fill the whole domain;
2) every internal surface $\mathcal{A}_{I,J}$ must be common to two adjacent control volumes; and
3) substance fluxed out of one volume must be fluxed into the next so that net substance is neither gained nor lost in the fluxing process.
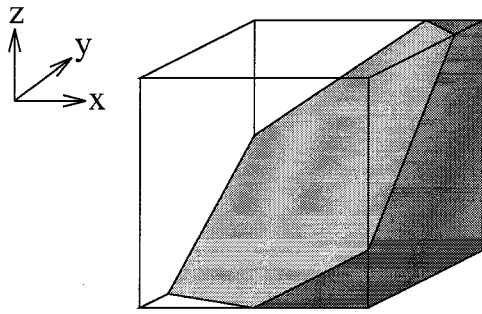
FIG. 2. A cell being cut by topography. The volume of the shaved cell, $\mathcal{V}_{i,j,k}$, is smaller than that of the unshaved cell, and the area of the faces of exchange between neighboring cells are also reduced.

   Budgeting over volumes using the divergence of fluxes naturally leads to a staggered grid; the fluxes are defined on the faces of the volumes analogous to the Arakawa C grid. Such an arrangement of flux quantities and volume-mean quantities is also necessary if discrete forms are to retain conservation properties, as will be discussed later.

   In general, the control volumes can take on any shape and be structured or unstructured, but here we consider the cells to be regular boxes in the physical coordinate system arranged in a logical manner. Each unshaved cell is defined as the volume contained between six surfaces where the surfaces are aligned with the chosen coordinate system: for example, the cell contained by the intersection of the six surfaces

$$x = x_{i-1/2}, \quad x = x_{i+1/2}, \quad y = y_{j-1/2}, \quad y = y_{j+1/2},$$

$$z = z_{k-1/2}, \quad \text{and} \quad z = z_{k+1/2},$$

has volume

$$\mathcal{V}_{i,j,k} = (x_{i+1/2} - x_{i-1/2})(y_{j+1/2} - y_{j-1/2})(z_{k+1/2} - z_{k-1/2})$$

$$= \Delta x_i \Delta y_j \Delta z_k.$$

We imagine that the "grid" of regular cells fills the physical domain without distortion so that the solid boundary of the ocean basin freely intersects those cells which abut it, as sketched in Figs. 1c and 2. The shaded area indicates solid land and the open space indicates water. The model variables are thus arranged as if they were on a regular grid. However, one should not think of model variables as carried at a regular grid of points as in a finite-difference model. In the finite-volume approach, the model variable is defined as the volume mean over a model cell. In the case where the topography intersects the model cell above the middle, no special consideration is needed; the mean depth ($v^{-1}\int z \, d\mathcal{V}$) of the cell is simply changed accordingly.

   Since the advective flux normal to a boundary vanishes, the shape of the solid bounding surface does not enter the advective budget. Thus, cells abutting a solid boundary may take on more complex geometries without introducing auxiliary terms or equations for each cell. The cell topology can be described with seven parameters; a volume and six surface areas. Figure 3 shows the six areas of open exchange corresponding to the shaved cell in Fig. 2. With zero normal flux at solid boundaries, the budget for volume-mean quantities is determined completely by the fluxes through the open areas of each face and the volume of water within the volume. Boundary conditions that involve nonzero normal fluxes can be written as effective volume-mean source terms (Q) but may demand a more complete description of the surface.[2]

a. Finite-volume continuity and tracer advection equations

   Application of the discrete finite volume equation (3) in three spatial dimensions gives

$$\mathcal{V}_{i,j,k}\frac{\partial}{\partial t}\phi_{i,j,k} + \mathcal{A}_{x_{i+1/2,j,k}}F_{x_{i+1/2,j,k}} + \mathcal{A}_{y_{i,j+1/2,k}}F_{y_{i,j+1/2,k}}$$

$$+ \mathcal{A}_{z_{i,j,k+1/2}}F_{z_{i,j,k+1/2}} - \mathcal{A}_{x_{i-1/2,j,k}}F_{x_{i-1/2,j,k}} - \mathcal{A}_{y_{i,j-1/2,k}}F_{y_{i,j-1/2,k}}$$

$$- \mathcal{A}_{z_{i,j,k-1/2}}F_{z_{i,j,k-1/2}} = \mathcal{V}_{i,j,k}Q_{i,j,k},$$

which, using the discrete notation of Arakawa (see appendix A), can be written more succinctly, thus

---

[2] For example, heat conduction across the surface would require that the area of the solid surface be supplied as a parameter. The parameterization of frictional effects might also include a curvature or roughness parameter as used in some atmospheric models.
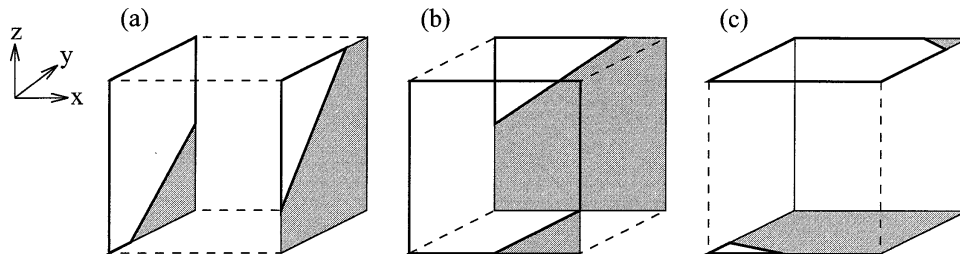

FIG. 3. Properties can flux into the volume $\mathcal{V}_{i,j,k}$, of the shaved cell, through the open faces of exchange (shown in pairs). Advective fluxes through the solid surface are zero. Each face is common to two neighboring volumes. The pairs shown in (a), (b), and (c) are labeled $A_{x_{i\pm1/2,j,k}}$, $A_{y_{i,j\pm1/2,k}}$, and $A_{z_{i,j,k\pm1/2}}$, respectively.

$$\mathcal{V}\frac{\partial}{\partial t}\phi + \delta_x(\mathcal{A}_x F_x) + \delta_y(\mathcal{A}_y F_y) + \delta_z(\mathcal{A}_z F_z) = \mathcal{V}Q. \quad (7)$$

The discrete equation for a conservative tracer θ is then obtained by setting $\phi = \theta$, $Q = 0$ and supposing that **F** contains both the advective flux $\boldsymbol{v}\theta$ and diffusive flux **D** (here we will assume that there is no diffusive flux across the solid boundary):

$$\mathcal{V}\frac{\partial}{\partial t}\theta + \delta_x(\mathcal{A}_x u\bar{\theta}^x + \mathcal{A}_x D_x) + \delta_y(\mathcal{A}_y v\bar{\theta}^y + \mathcal{A}_y D_y)$$

$$+ \delta_z(\mathcal{A}_z w\bar{\theta}^z + \mathcal{A}_z D_z) = \mathcal{V}Q. \quad (8)$$

The continuity equation is obtained by setting $\phi = Q = 0$ and $\mathbf{F} = \mathbf{v}$ to give

$$\delta_x(\mathcal{A}_x u) + \delta_y(\mathcal{A}_y v) + \delta_z(\mathcal{A}_z w) = 0. \quad (9)$$

Note that the flux divergence operator in (8) is very similar to the divergence operator in the continuity equation. This property is now made use of when we consider conservation of higher moments.

b. Conservation properties of the discrete tracer equations

The net amount of tracer is identically conserved by the discrete advection operator (8) because it has been written as the divergence of a flux. Because of the way we have chosen to average θ, it turns out that (8) also conserves the domain average of the second moment (θ^2), in a direct analogy with the continuous equations:

$$\frac{D}{Dt}\left(\frac{1}{2}\theta^2\right) = \theta\frac{D}{Dt}\theta = 0.$$

For global conservation of the second moment, we must be able to write the advective terms in (8), when multiplied by θ, as the divergence of a flux:

$$\theta[\delta_x(A_x u\bar{\theta}^x) + \delta_y(A_y v\bar{\theta}^y) + \delta_z(A_z w\bar{\theta}^z)]$$

$$= \delta_x\left(A_x u\frac{1}{2}\wr\theta\wr_x^2\right) + \delta_y\left(A_y v\frac{1}{2}\wr\theta\wr_y^2\right) + \delta_z\left(A_z w\frac{1}{2}\wr\theta\wr_z^2\right)$$

$$+ \frac{1}{2}\theta^2[\delta_x(A_x u) + \delta_y(A_y v) + \delta_z(A_z w)],$$

a result derived in the appendix. Here $\wr\theta\wr_x^2 \equiv \theta_{i-1/2}\theta_{i+1/2}$ is the geometric product between two neighboring points. The last term vanishes due to (9). The remaining term on the right-hand side is written as the divergence of an advective flux [analogous to $\nabla\cdot(\frac{1}{2}\theta^2\mathbf{u})$ in the continuum] and so also vanishes on application of boundary conditions when summed over the whole model.

3. Representation of topography

So far we have described a finite-volume approach that is ideally suited for arbitrary geometries. We now
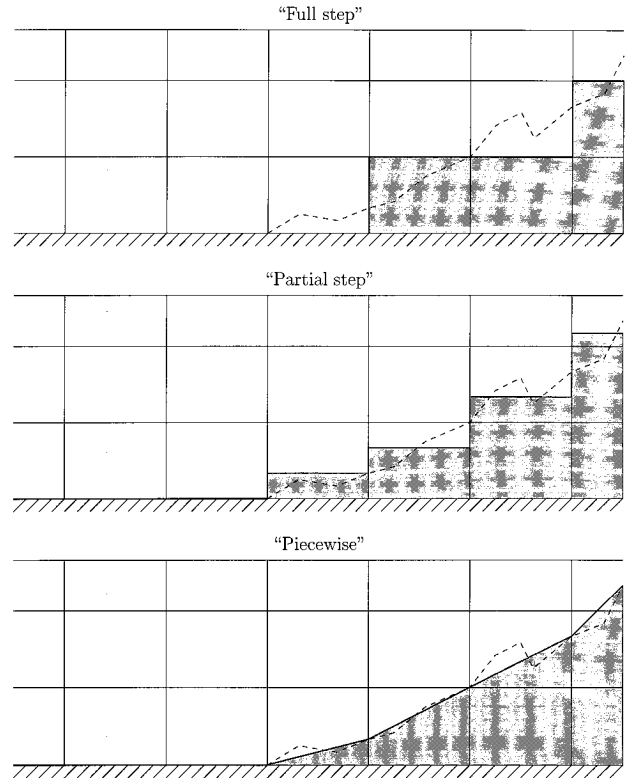

FIG. 4. The representation of hypothetical topography (dashed line) in a height coordinate ocean model. In the "full step" approach, that of conventional finite-difference models, the bottom depth is chosen to coincide with the model grid. In the "partial step" representation the thickness of the volumes abutting the bottom can be adjusted to match the topography. In both the "full" and "partial step" methods, the bottom depth is discontinuous. The "piecewise" representation assumes a constant linear slope within each cell. The bottom depth is then continuous, though its gradient is not.

discuss the manner in which we represent topography by shaving those volumes. To facilitate this discussion, we consider a two-dimensional problem in the y–z plane. Figure 4 shows some possible approximate representations of a hypothetical topographic surface, shown as a dashed line. The position of the approximate surface can then be used to "shave" the model cells.

In the conventional finite-difference approach, as employed in the Geophysical Fluid Dynamics Laboratory model (Bryan 1969), for example, the depth of the bottom is rounded to the nearest model depth to form "full steps." This is the lowest-order representation of the ocean bottom. Neither the volume of the water column nor the cross-sectional area presented to the flow are accurately approximated unless the ocean bottom happens to be flat and lie at a model depth!

In the "partial step" approach, the bottom surface can take any intermediate depth within the cell, thus capturing the volume of the water column more accurately. The bottom cell of each column in the model can have its volume appropriately chosen but steps are still present. This approach was discussed by Cox (1977)
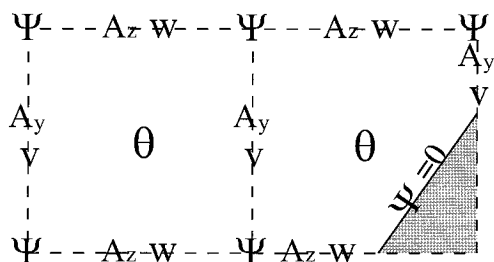
FIG. 5. Arrangement of streamfunction Ψ, passive tracer θ, and advecting flow v and w.

and used by Semtner and Mintz (1977) (see their Fig. 2), Maier-Reimer and Mikolajewicz (1992), and D. S. Stevens and S. Maskell (1996, personal communication). In both "step" methods, the bottom discontinuously jumps. The size of the steps is less in the "partial step" method and is therefore perhaps more desirable.

The "piecewise" slope representation assumes a constant slope within each cell and the face coincident with the bottom is allowed to intersect the vertical edges at any point. As can be seen in Fig. 4, this is a better approximation to the "true" surface except in local regions of high curvature (i.e., the topography has large subgrid-scale variations). Moreover, the bottom depth is now continuous and ought to lead to "smoother" solutions. We now go on to compare the results of using these three representations of the topography: the "full step," "partial step," and "piecewise slope" methods.

An illustration: Advection of a passive tracer in 2D

The problem we pose is the advection of a passive tracer by a *prescribed* nondivergent flow. The two conservation laws for the discrete volumes are the continuity and tracer advection equations. The discrete two-dimensional continuity equation is

$$\delta_y(\mathcal{A}_y v) + \delta_z(\mathcal{A}_z w) = 0. \tag{10}$$

A streamfunction can be constructed that exactly satisfies (10):

$$v = \frac{\delta_z \Psi}{\mathcal{A}_y}, \qquad w = -\frac{\delta_y \Psi}{\mathcal{A}_z}, \tag{11}$$

suggesting that Ψ be chosen to lie at the corners of the model cells (see Fig. 5). The discrete two-dimensional tracer equation is

$$\mathcal{V}\frac{\partial \theta}{\partial t} + \delta_y(\mathcal{A}_y v \bar{\theta}^y) + \delta_z(\mathcal{A}_z w \bar{\theta}^z) = 0. \tag{12}$$

The calculation is simplified by the flow being prescribed. We have also chosen not to represent any subgrid-scale terms and to assume that there are no sources and sinks; this will test the advection operator in the extreme limit of no dissipation.

We impose a sheared zonal flow over a Gaussian topographic feature. All variables and parameters are non-

dimensional. The channel is of unit depth ($-1 \le z \le 0$) and of length 2 ($-1 \le y \le +1$) and is periodic in y. The height of the topographic feature is given by

$$h(y) = h_o e^{-(y/\lambda)^2}, \tag{13}$$

where λ is the decay scale. The nondivergent shear flow is specified by

$$\Psi(y, z) = (1 - \zeta)^2 \text{ where } \zeta = z/[h(y) - 1], \tag{14}$$

so that $\Psi(y, z = 0) = 1$ and $\Psi(y, z = h - 1) = 0$. The initial conditions are $\theta(y, z) = 1 + z$. The bump has height $h_o = 1/2$ and decay scale $\lambda = 1/4$. There is no explicit diffusion. We first use 16 points in the horizontal and eight levels in the vertical so that the aspect ratio of an unshaved model cell is unity.

Figure 6 shows the streamfunction Ψ (fixed in time) and tracer θ at $t = 0.3$ for three realizations of the finite-volume representation of the smoothly varying bottom topography: (a) full step, (b) partial step, and (c) piecewise linear slope. The common feature in the streamfunction is a compression of the streamlines over the bump. Vertical motion should be confined to the slopes of the bump. In the full-step representation, the top of the bump is crudely represented as a level plateau. The vertical velocity is consequently zero above the center and elsewhere is compressed into vertical bands above each step. The same is true of the streamfunction in the partial step calculation, but the discontinuities are less severe. In the piecewise slope calculation, the streamfunction follows the smoothly varying bottom depth with no discontinuities.

The common feature in the tracer field of each calculation is a column of high values that have been swept off to the right from above the bump. The flow has also sheared the feature as it carries it downstream. Any discontinuities in the streamfunction, seen as bands of upwelling, will lead to grid-scale noise in the tracer field. This effect can be seen most prominently in the full-step calculation. Upstream of the bump, the noise takes on the characteristic up–down grid-scale pattern. The amplitude of the noise is much reduced in the partial-step calculation and barely discernible in the piecewise slope calculation. Remember that these calculations have no explicit diffusion; in practice such noise might be removed by explicit diffusion or a diffusive advection scheme.

If we increase the horizontal resolution the aspect ratio of unshaved model cells will approach the typical aspect ratio of general circulation models. Figure 7 shows the same scenario using twice as many points (32) in the horizontal as in Fig. 6.

The full-step representation is even less accurate now, representing the slope as a series of level plateaus. The discontinuities in the streamfunction are now over narrower bands, enhancing the vertical velocity. The spurious oscillations in the tracer field dominate the solution. In contrast, the partial-step and piecewise linear slope cases have improved, the

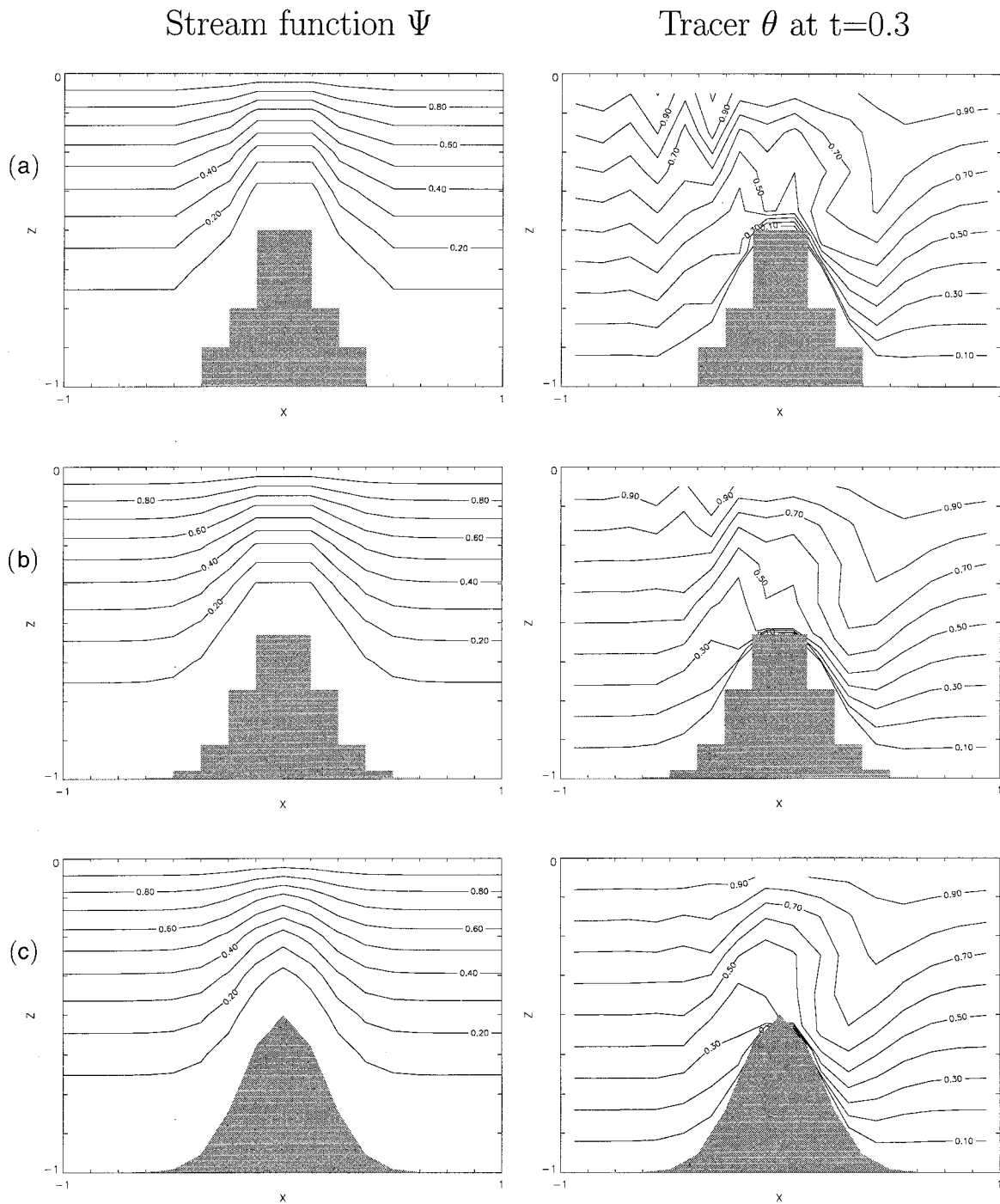## Stream function Ψ

Tracer θ at t=0.3

FIG. 6. Streamfunction Ψ and passive tracer θ at time $t = 0.3$ (time is normalized by the advective timescale) for three renditions of zonal flow over a Gaussian bump. The bump has height $h_o = 1/2$ and exponential decay scale 1/4. The model resolution is $\Delta y = 1/8$ and $\Delta z = 1/8$. The bump is represented in (a) by full-step, (b) by partial-step, and (c) by linear piecewise methods.

streamfunction in the partial step is smoother than before, and the noise level is consequently much reduced. Indeed, the piecewise slope calculation has almost indiscernible noise levels, which suggests that, in the limit of high resolution, the piecewise slope solution approaches the continuum faster than the par-

tial-step solution. This could also be deduced from the actual representation of the slope; the partial-step method has an error that decreases linearly with N, the number of grid points in the horizontal, while the piecewise slope decreases quadratically (N^2).

This example demonstrates the inadequacy of the

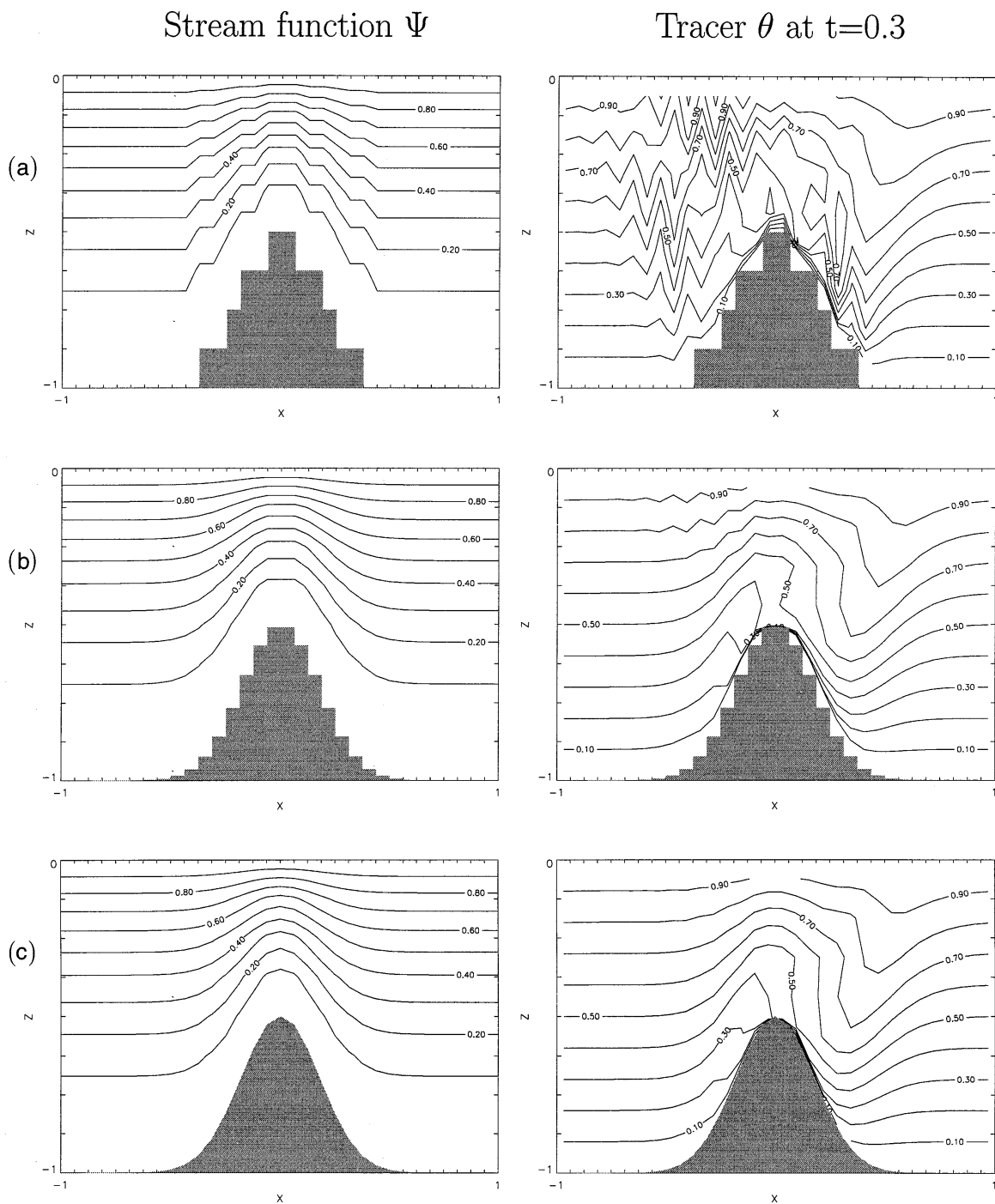## Stream function Ψ Tracer θ at t=0.3

FIG. 7. As in Fig. 6 but at twice the horizontal resolution. Here, $\Delta y = 1/16$ and $\Delta z = 1/8$.

full-step representation of topography for the simple problem of passive tracer advection by a steady flow field. The spurious oscillations in the tracer field become more prominent with increasing horizontal resolution (i.e., as the flat plateaus span an increasing number of grid points). The difference in volumes and areas between the partial-step and trapezoidal representations vanishes as the horizontal resolution becomes infinitesimal. The partial-step method does appear adequate at high horizontal resolution, but the piecewise linear slope method is clearly superior, especially at coarse resolution.

The noisiness of the tracer fields in the above experiments is a numerical response to the discontinuities
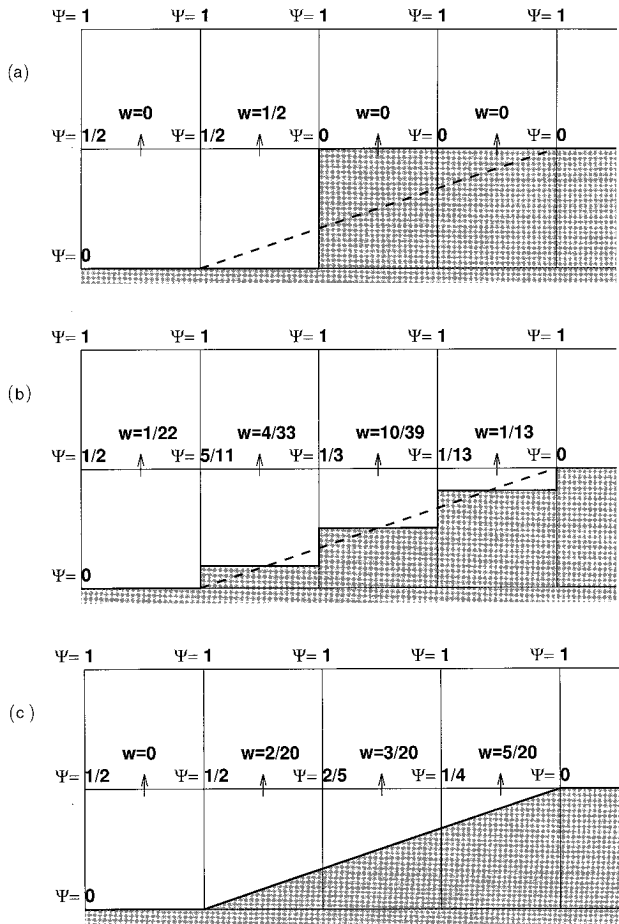
FIG. 8. Three idealizations of barotropic flow across a hypothetical slope (dashed line). The transport streamfunction is given by $\Psi = 1 - z/H$ where we have assumed unit depth and unit horizontal grid spacing. In the "full step" approach (a), w_z is zero everywhere except at a single model point. The "partial step" (b) and "piecewise linear" (c) approaches both have smoother w fields, where the upwelling is spread over three or four points.

in the advecting flow, which in turn arise from the discontinuities in the bottom profile. To further illustrate the nature of the difference between the full-step and shaved-cell approaches, we consider the simple case of barotropic flow across the hypothetical slope shown in Fig. 8. In the full-step approach (Fig. 8a), the slope is represented by a single step. The vertical velocity is zero everywhere except for the model point upstream of the step and hence appears discontinuous to the model. Consider next the piecewise linear approach shown in Fig. 8c. Here the model sees an *exact* representation of the linear slope so the vertical transport is appropriately spread out over the length of the slope. The vertical velocity field is subsequently smoother than in the full-step case. Finally, consider the partial-step approach shown in Fig. 8b. Here, we choose the model depths to exactly represent the volume of water columns. As a result, the far left column of the model sees a small barrier, which forces a vertical motion. The vertical ve-
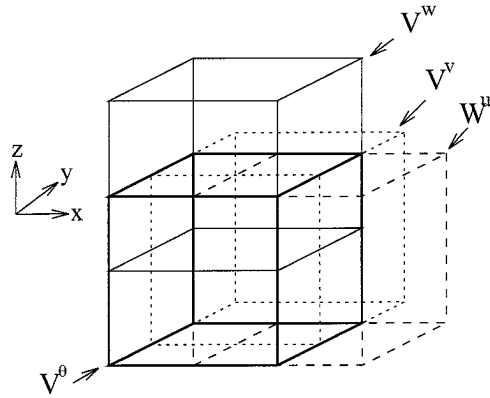

FIG. 9. The control volumes for the u, v, and w variables are staggered in space relative to the tracer control volume $\mathcal{V}^\theta$.

locity is subsequently spread out over four model points and is thus smoother, though less accurate, than in the piecewise linear approach.

4. Discretization of the incompressible Boussinesq equations using finite volumes

Instead of prescribing the flow, we now wish to find it by stepping forward the hydrodynamical equations. The incompressible Boussinesq equations for oceanic motion consist of the incompressibility condition (nondivergence of the flow), two horizontal momentum equations, one vertical momentum equation (which may take the form of hydrostatic balance), prognostic equations for the potential temperature and salinity, and an equation of state. The equations are written out in full in Marshall et al. (1997a).

As we have seen, discrete forms of the continuity and tracer equations (heat and salt) are obtained by integrating over the volume of the tracer cells; we label these cells with a superscript, θ. Each tracer cell has associated with it a volume $\mathcal{V}^\theta$ and three areas A_x^θ, A_y^θ, A_z^θ for the eastern, northern, and upper faces, respectively. Only three face areas are needed since each face is common to two cells. Cells that abut the solid boundary are shaved to fit the boundary by, as before, appropriately modifying the volume and areas. No extra parameters are needed to describe the shaved cell as long as the flux normal to the solid surface is zero.

The control volumes for the velocity variables u, v, and w are shifted relative to the tracer volumes and are sketched in Fig. 9. For unshaved cells, the volumes and areas of the cells can be readily deduced since they are regular. Each of the variables u, v, and w has associated with it a volume and three face areas, identified using the appropriate superscript. The discrete momentum equations are then found by applying the finite-volume formulation of section 2. The overall discretization, including a discussion of hydrostatic, nonhydrostatic, and quasi-hydrostatic forms, is given in Marshall et al. (1997b), the details of which will not be repeated here.
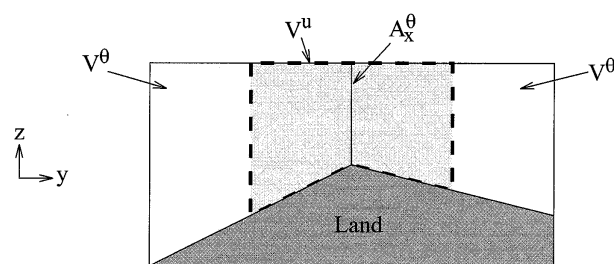
FIG. 10. Assuming piecewise slopes within the two neighboring tracer cells (labeled V^θ), the bottom within the consistent u volume (labeled V^u) is constructed from two sections of piecewise slope.

However, one important question is, what shapes do the momentum volumes take in the case of shaved cells? Consider, for example, the two neighboring tracer cells in Fig. 10 in which we have assumed a piecewise slope representation of the topography. The thick dashed line outlines an obvious choice for the u volume even though it has a different form than for an individual tracer volume; the surface defining the base of the u volume is formed from *two* piecewise slopes, whereas the bottom surface of tracer volumes is represented using only one piecewise slope.

In the finite-volume formulation, the conservation properties are readily obtained for the first moments of the flow and tracers. However, as in the implementation of Marshall et al. (1997a), we can also retain conservation of second moments if the volumes are chosen carefully. This is achieved in the tracer equations by using centered, unweighted interpolation. As we now go on to discuss, special consideration of the discretization of the momentum equations, and in particular pressure gradient forces, is required to retain kinetic energy conservation. This has ramifications for the form of the elliptic problem. We describe these implementation details next.

a. Form of the pressure gradient and elliptic equation

The elliptic equation for pressure is formed by taking the divergence of the momentum equations and invoking continuity:

$$\left.\begin{array}{r} \dfrac{\partial}{\partial t}\mathbf{v} + \boldsymbol{\nabla}P = \mathbf{G} \\[2mm] \boldsymbol{\nabla}\cdot\mathbf{v} = 0 \end{array}\right\} \Rightarrow \nabla^2 P = \boldsymbol{\nabla}\cdot\mathbf{G}, \qquad (15)$$

where $P = p/\rho_o$ and all terms in the momentum equations have been collected into the vector $\mathbf{G}$. When the momentum equation is discretized in time, the pressure gradient force can be thought of as that force required to ensure nondivergence at the next time step. The pressure field is unique to within a constant of integration (homogeneous Neumann boundary conditions are implicit in the finite-volume formulation). The pressure gradient force, with zero curl, which guarantees non-

divergence, is unique, as can be illustrated as follows. Expressing (15) in terms of the pressure gradient force $\mathbf{F}_p = \boldsymbol{\nabla}P$:

$$\left.\begin{array}{r} \dfrac{\partial}{\partial t}\mathbf{v} + \mathbf{F}_p = \mathbf{G} \\[2mm] \boldsymbol{\nabla}\cdot\mathbf{v} = 0 \end{array}\right\} \Rightarrow \left\{\begin{array}{l} \boldsymbol{\nabla}\cdot\mathbf{F}_p = \boldsymbol{\nabla}\cdot\mathbf{G} \\[2mm] \boldsymbol{\nabla}\times\mathbf{F}_p = 0, \end{array}\right. \qquad (16)$$

where we have noted that $\mathbf{F}_p$, because it can be written as the gradient of a scalar, the pressure, has zero curl. There is only one field of force $\mathbf{F}_p$ that has divergence $\boldsymbol{\nabla}\cdot\mathbf{G}$ and zero curl. Because it is only the pressure gradient *force* that appears in the momentum equations, there is a certain flexibility in our choice of discretization of it; if we change our discretization of $\boldsymbol{\nabla}P$ the discrete form of the elliptic operator may change but the same discrete pressure gradient will be implied by that field. We are therefore at liberty to modify our choice of discretization so that it leads to a simple elliptic equation. We thus simply write, for example, the zonal momentum equation as

$$\frac{\partial}{\partial t}u + \frac{1}{\Delta x^u}\delta_x P = G^u,$$

where Δx^u is some (as yet undefined) length over which the pressure gradient is measured. When we consider the kinetic energy balance we will find Δx^u has to be appropriately chosen to ensure conservation. The above discretization of the pressure gradient terms also ensures that the elliptic operator remains symmetric and so standard conjugate gradient methods can be used to solve it. We choose the preconditioned conjugate gradient algorithm over multigrid methods because it can readily handle an irregular domain. Details of the implementation of this algorithm and its mapping on to parallel computer architectures can be found in Marshall et al. (1997a).

b. Energy conservation

Some terms in the finite-volume momentum equations need to be interpolated from the volume-mean quantities either because they are needed at faces (e.g., velocities in advection terms) or because they are needed in a different volume (e.g., fv Coriolis term in the u cell). We use centered (i.e., unweighted) interpolation for these terms. This ensures that in the interior of the ocean, the finite-volume discretization recovers the second-order finite-difference discretization of Arakawa and Lamb (1977). This particular discretization has the property of conserving first and second moments of all quantities in a manner analogous to the continuous equations. To reproduce analogs of these conservative properties near the boundaries, we must carefully consider each term in the momentum equations.

The nonlinear terms (e.g., $\mathbf{F}_u = \mathbf{v}u$) ought to conserve total kinetic energy. If we discretize thus,

$$\oint_{\mathcal{A}} \mathbf{F}_u \cdot d\mathcal{A} = \delta_x(U^*\bar{u}^x) + \delta_y(V^*\bar{u}^y) + \delta_z(W^*\bar{u}^z), \quad (17)$$

where U^*, V^*, and W^* have units of area times velocity, then it can be shown (see appendix B) that to ensure global conservation of u^2, the $\mathbf{V}^*$'s themselves must satisfy a nondivergence condition:

$$\delta_x U^* + \delta_y V^* + \delta_z W^* = 0. \quad (18)$$

Since the flow (u, v, and w) satisfies continuity over a tracer volume (9), this requirement can be satisfied by choosing

$$U^* = \overline{\mathcal{A}_x^\theta u}^x \qquad V^* = \overline{\mathcal{A}_y^\theta v}^x \qquad W^* = \overline{\mathcal{A}_z^\theta w}^x. \quad (19)$$

Similar quantities are invoked for the y and z momentum equations where the $-x$ averaging is replaced with $-y$ and $-z$.

In the continuum, the Coriolis terms do not generate kinetic energy since $\mathbf{v} \cdot (f\mathbf{k} \times \mathbf{v}) = 0$. The discretized Coriolis terms can be chosen to imply no *net* kinetic energy generation (i.e., when integrated over the whole model) if they are written thus,

$$\int_{\mathcal{V}^u} fv\, d\mathcal{V} = \overline{f\mathcal{V}^\theta \bar{v}^x}^x$$

$$\int_{\mathcal{V}^v} fu\, d\mathcal{V} = \overline{f\mathcal{V}^\theta \bar{u}^{x}}^y.$$

The discrete analog of the generation term does not vanish locally but has the form

$$\overline{u\overline{f\mathcal{V}^\theta \bar{v}^x}^x} - \overline{v\overline{f\mathcal{V}^\theta \bar{u}^x}^y}^y = \delta_x[u\delta_x(f\mathcal{V}^\theta \bar{v}^y)]$$
$$- \delta_y[v\delta_y(f\mathcal{V}^\theta \bar{u}^x)].$$

However, since the right-hand side is the divergence of a flux, its global sum vanishes.

In the continuum, conservation of total kinetic energy also depends on the identity

$$\mathbf{v} \cdot \boldsymbol{\nabla}P = \boldsymbol{\nabla} \cdot (\mathbf{v}P) - P\boldsymbol{\nabla} \cdot \mathbf{v} = \boldsymbol{\nabla} \cdot (\mathbf{v}P). \quad (20)$$

The discrete finite-volume analog is

$$\overline{\mathcal{V}^u u \frac{\delta_x P}{\Delta x^u}}^x + \overline{\mathcal{V}^v v \frac{\delta_y P}{\Delta y^v}}^y + \overline{\mathcal{V}^w w \frac{\delta_z P}{\Delta z^w}}^z$$
$$= \delta_x \left(\frac{\overline{P}^x \mathcal{V}^u u}{\Delta x^u} \right) + \delta_y \left(\frac{\overline{P}^y \mathcal{V}^v v}{\Delta y^v} \right) + \delta_z \left(\frac{\overline{P}^z \mathcal{V}^w w}{\Delta z^w} \right)$$
$$- P \left(\delta_x \frac{\mathcal{V}^u u}{\Delta x^u} + \delta_y \frac{\mathcal{V}^v v}{\Delta y^v} + \delta_z \frac{\mathcal{V}^w w}{\Delta z^w} \right), \quad (21)$$

where Δx^u, Δy^v, and Δz^w are the effective distances over which the pressure gradient is evaluated. The last term should vanish by continuity but will not do so unless we choose

$$\Delta x^u = \frac{\mathcal{V}^u}{A_x^\theta} \qquad \Delta y^v = \frac{\mathcal{V}^v}{A_y^\theta} \qquad \Delta z^w = \frac{\mathcal{V}^w}{A_z^\theta}. \quad (22)$$

Thus, to ensure good energetic credentials in the discrete momentum equation, we choose Δx^u as given above where $\mathcal{V}^u$ is defined as in Fig. 10. The complete spatial discretization of the zonal momentum equation is then

$$\mathcal{V}^u \frac{\partial}{\partial t}u + \delta_x(\overline{\mathcal{A}_x^\theta u}^x u) + \delta_y(\overline{\mathcal{A}_y^\theta v}^x u) + \delta_z(\overline{\mathcal{A}_z^\theta w}^x u)$$

$$- \overline{f\mathcal{V}^\theta \bar{v}^y}^x + \frac{1}{\Delta x^u}\delta_x P = \cdots$$

and similarly for the meridional and vertical momentum equations.

c. Gravity wave noise induced by "step" topography

Continuing the theme of comparing solutions using the "step" and "shaved cell" representation of topography, we present a further two-dimensional example, this time using the hydrodynamical model of Marshall et al. (1997a) to study the influence of topography on the flow (previously, the flow was specified). We consider a zonally averaged channel, the bottom of which is inclined to the horizontal. A (zonal) wind-stress-driven meridional circulation induces downwelling on the deep side of the channel and upwelling on the shallow side (see Fig. 11). The deep return meridional flow, moving over the bottom slope, must match the surface Ekman transport set by the wind.

The model is confined to the y–z plane by setting all derivatives in the x direction to zero. To isolate the generation of gravity waves over step topography from the numerical issues described in section 3a, we have switched off all nonlinearity in the code so that the buoyancy equation is simply $\partial b/\partial t = -wN^2$, where N^2 is constant. The wind forcing is given a half sinusoidal profile with magnitude 2 dyn. The stratification is $N = 20f$, where the Coriolis parameter is a constant, $f = 1 \times 10^{-4}$ s^{-1}.

Each of the following experiments attempts to model the effect of a constant bottom slope in a channel of width 1000 km ($\Delta x = 50$ km), such that $H(y = 0$ km$) = 4000$ m and $H(y = 1000$ km$) = 3000$ m. Figure 11 shows the meridional circulation in a four-level model ($\Delta z = 1000$ m) at an instant in time, 2.5 inertial periods ($t = 5\pi/f$) into the model spinup (in this case, no bottom stress is specified so the model would actually spinup indefinitely). The first panel (Fig. 11a) shows the model solution when a stepwise approach is used. Halfway along the bottom, the meridional flow "hits" the wall of the step and is forced to turn upward. This collision with a solid wall generates gravity waves that radiate away from the region of the step. The kinks in the instantaneous streamfunction are the manifestation of these topography-generated gravity waves.

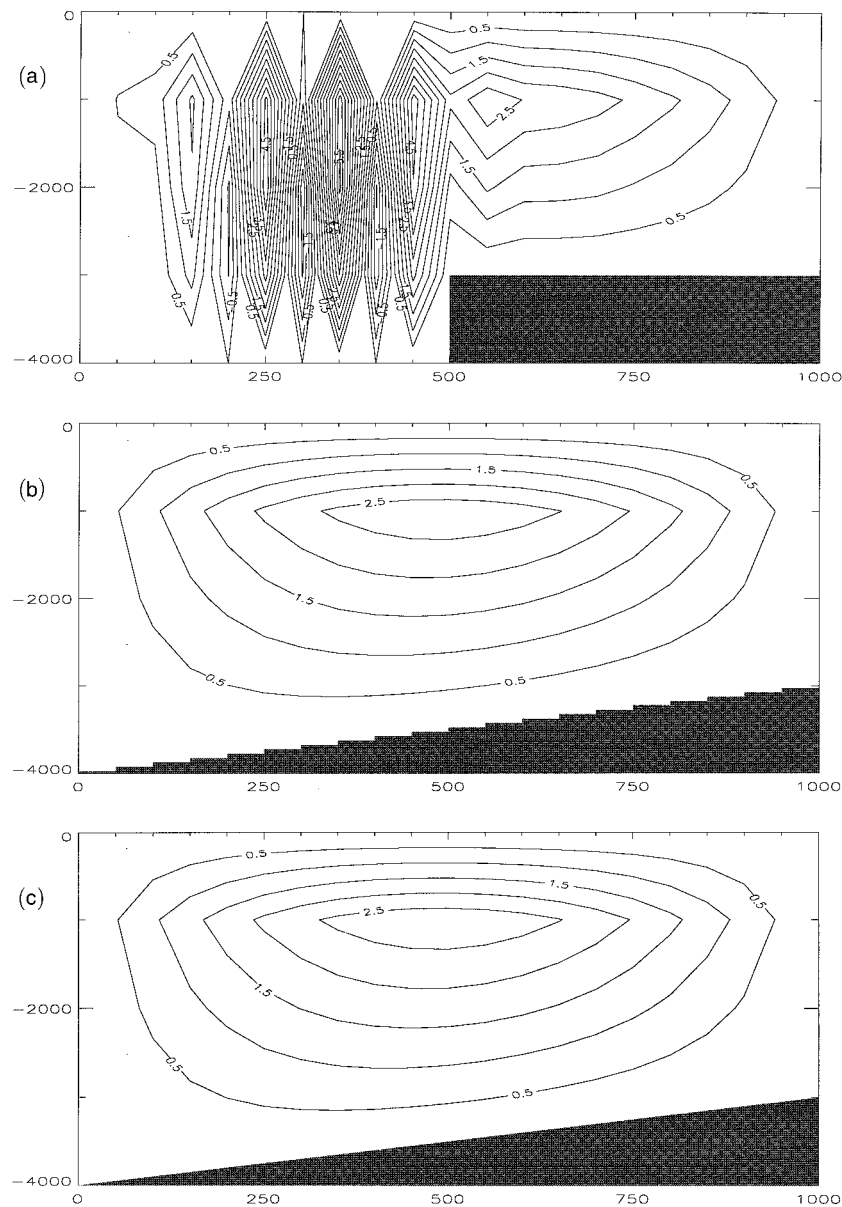In contrast, the partial-step (Fig. 11b) and piecewise

FIG. 11. Streamfunction Ψ at time $t = 5\pi/f$ (i.e., 2.5 inertial periods) for three simulations of meridional circulation over a shallow meridional slope across a channel. The solutions (a), (b), and (c) were obtained with the full-step, partial-step, and piecewise linear representations, respectively. There are four levels in the vertical so the full-step calculation (a) sees the slope as only a single step. The contour interval (0.5 Sv) is the same in all plots.

(Fig. 11c) representations have no such problems (the slope is represented exactly by the piecewise method because the slope is constant). In both cases, the meridional circulation smoothly follows the sloping boundary ($w = -v\partial H/\partial y$). These two solutions appear to be nearly identical because the bottom depths are so similar; the difference between partial step and piecewise linear representations is insignificant for shallow slopes.

With increased vertical resolution (eight levels, $\Delta z = 500$ m), the amplitude of the topography-generated gravity waves is reduced (see Fig. 12a). However, there

are now two steps and therefore double the source of gravity wave energy. Furthermore, a gently rising motion of fluid near the bottom boundary is absent and replaced by discontinuous jumps. Again, the partial-step and piecewise linear representations have none of these problems.

These experiments were intentionally carried out with a linear model to isolate the problem of topographically generated (gravity wave) noise in dynamical models from the issues raised in the passive tracer experiment. It is quite likely that the combination of
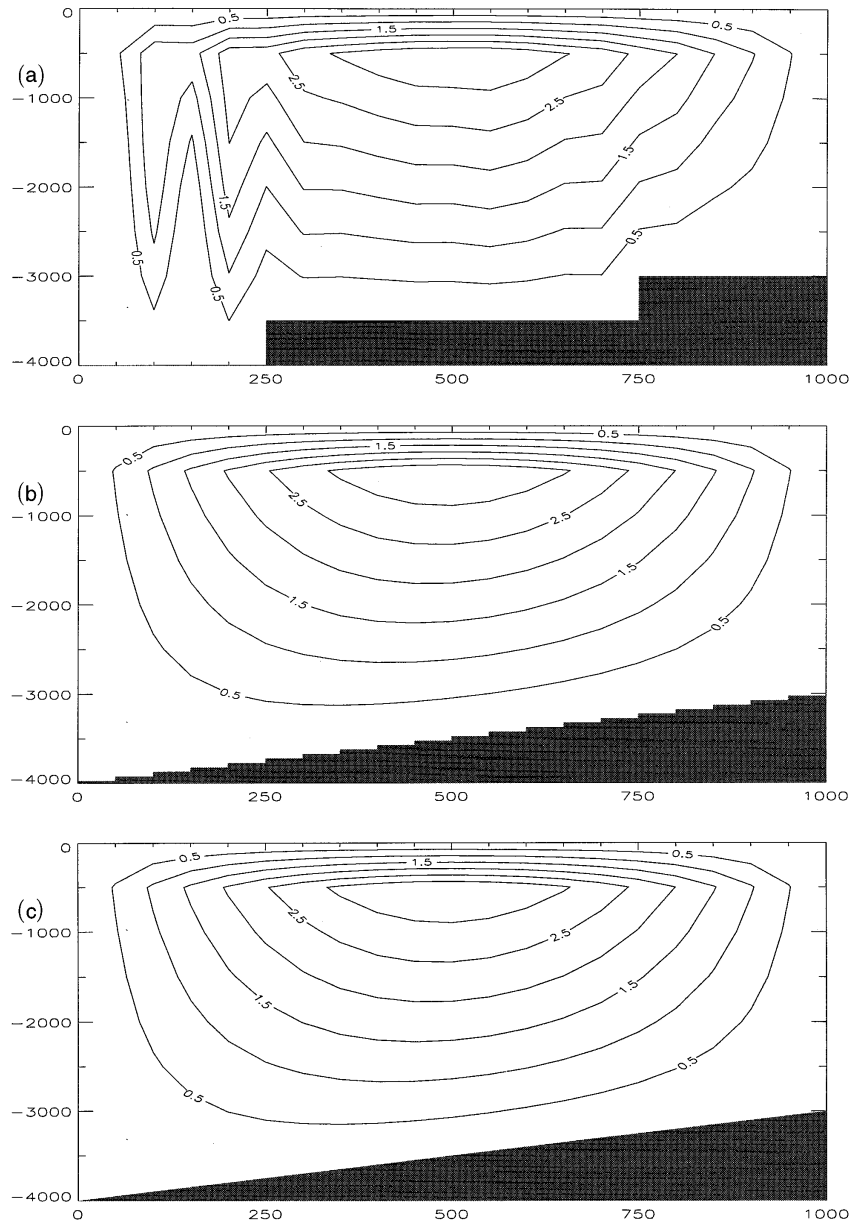
FIG. 12. As for Fig. 11 but with eight levels in the vertical.

noisy advecting fields and noisy active tracer fields would present even more of a problem in higher–Rossby number flows.

5. Further oceanic illustrations

The discretization outlined in the previous section was used to formulate the 3D numerical model of Marshall et al. (1997a). Here we further test the representation of topography using shaved cells as an alternative to the conventional stepwise representation in simulations of the large-scale ocean circulation.

The first experiment highlights the importance of ac-

curately representing shallow slopes in dynamical models. The second set of experiments attempts to test the approach in the presence of order 1 topography through direct comparison with a terrain-following coordinate model. We also study how the various schemes behave as their respective resolutions are increased.

a. Topographic β effect at large horizontal scales

Steady, inviscid, and weak flow of a homogeneous rotating fluid must, by the Taylor–Proudman theorem, follow contours of f/H, where f is the Coriolis parameter and H is the fluid depth. Variations in f/H can be due

TABLE 1. Parameters for the two experiments to model planetary (I) and topographic (II) β effects ($f_o = 1 \times 10^{-4}$ s^{-1}, $\beta = 1.6 \times 10^{-11}$ s^{-1} m^{-1}, $H_o = 4000$ m).

Experiment	I	II
Dimension for x (km)	0 to 2000	0 to 2000
Dimension for y (km)	−2000 to 2000	−2000 to 2000
Grid spacing Δx (km)	100	100
Grid spacing Δy (km)	100	100
Time step Δt (s)	3600	3600
Depth $H(y)$ (m)	H_o	$H_o/(1 + \beta y/f_o)$
Coriolis $f(y)$ (s^{-1})	$f_o + \beta y$	f_o
Horizontal viscosity A_H (m^2 s^{-1})	5000	5000

TABLE 2. Parameters for the SPEM comparison experiment. The resolution in the SPEM integration is approximate. A stretched coordinate was used to increase resolution over the bump.

	FVGCM	SPEM
Grid size ($N_x \times N_y$)	80×60	66×65
Zonal resolution Δx (km)	5	$4.375 \leq \Delta x \leq 8.125$
Meridional resolution Δy (km)	5	$3.281 \leq \Delta y \leq 6.094$
Nominal ocean depth H (m)	4500	4500
Height of bump h (m)	4050	4050
Length scale of bump L (km)	25	25
Stratification NH/fL	1.5	1.5
Barotropic in-flow u_o (cm s^{-1})	25	25
Horizontal dissipation $A_4 \nabla_h^4$ (m^4 s^{-1})	5×10^9	5×10^9
Vertical viscosity A_V ($\partial^2/\partial z^2$) (m^2 s^{-1})	10^{-3}	10^{-3}
Horizontal diffusion $\kappa_4 \nabla_h^4$ (m^2 s^{-1})	1×10^9	1×10^9
Vertical diffusion $\kappa_V(\partial^2/\partial z^2)$ (m^2 s^{-1})	10^{-5}	10^{-5}
Time step Δt (s)	600	432

to a variation in the planetary vorticity ($\partial f/\partial y = \beta \neq 0$) or to a sloping bottom.

On a β plane in a basin of constant depth H_o, the potential vorticity and its meridional gradient are

$$Q = \frac{f_o + \beta y}{H_o}; \qquad \frac{\partial Q}{\partial y} = \frac{\beta}{H_o}, \qquad (23)$$

while on an f plane with variable bottom depth $H(y)$:

$$Q = \frac{f_o}{H(y)}; \qquad \frac{\partial Q}{\partial y} = \frac{-f_o}{H_o^2}\frac{\partial H}{\partial y}. \qquad (24)$$

To obtain the same PV and PV gradient in both cases, $H(y)$ in (24) must vary thus,

$$H(y) = \frac{H_o}{1 + (\beta y/f_o)}. \qquad (25)$$

The model was configured for two experiments: the first (i) on a β-plane basin with a constant depth, H_o, the second (ii) on an f plane with a variable depth given by (25). We forced the model with the same wind stress in both calculations; $\tau^{(x)} = \tau_o \cos 2\pi y/L_y$, $\tau^{(y)} = 0$. The maximum wind stress was $\tau_o = 2$ dyn cm^{-2}. The horizontal viscosity A_H was chosen such that the Munk layer thickness $\delta_{Munk} \sim (A_H/\beta)^{1/3}$ was just resolved by the grid. All numerical parameters are summarized in Table 1 and were the same for both experiments.

The model was set up with one layer[3] and a regular Cartesian grid. The homogeneity of the layer is guaranteed if temperature and salt of the layer are initially homogeneous and there is no buoyancy forcing. In the second experiment, the shaved cells are invoked to represent the variable bottom depth. The same code is used for both calculations.

The barotropic streamfunction (depth-integrated transport) after one year is shown for each experiment in Fig. 13. The solutions are nearly identical. We conclude that the use of shaved cells endows the model with the ability to respond to the gentle topographic variations in a realistic way.

---

[3] With a "rigid-lid," the model then reduces to the barotropic equations.

b. Flow over a Gaussian bump

A direct comparison of the finite-volume model of Marshall et al. (1997a) with SPEM v3.0 (Haidvogel et al. 1991) was made possible by D. Goldner (MIT/WHOI Joint Program, 1995). He made numbers available from an experiment conducted using SPEM to study flow over a seamount (Fieberling, an amazing topographic feature in the Pacific Ocean that looks very much like a Gaussian bump!).

A Gaussian bump was placed in a periodic channel of width 300 km and length 400 km. The bump had a characteristic horizontal length scale of 25 km and was centered in the channel. It rose to a height of 90% the depth of the ocean (i.e., to within 450 m of the surface).

The finite-volume code was configured to match the SPEM integration as much as possible. SPEM (version 3.0) uses a spectral representation in the vertical and is formulated using σ coordinates as a vertical coordinate. Eight modes were used in SPEM and so eight levels in the vertical were chosen in the finite-volume model, equally spaced since the stratification was initially constant. The SPEM integration also used stretched coordinates in the horizontal to increase resolution over the bump. A horizontal resolution of 5 km was chosen for the finite-volume model as an approximate mean of the SPEM resolution (see Table 2).

SPEM used biharmonic dissipation, oriented along the sloping σ surfaces, with a damping timescale of 35 h on a length scale of 5 km. The same amount of biharmonic dissipation is used in the shaved cell calculations, but the operator acts along horizontal surfaces.

The models were initialized with a barotropic inflow of 25 cm s^{-1}. Both models are periodic but SPEM is
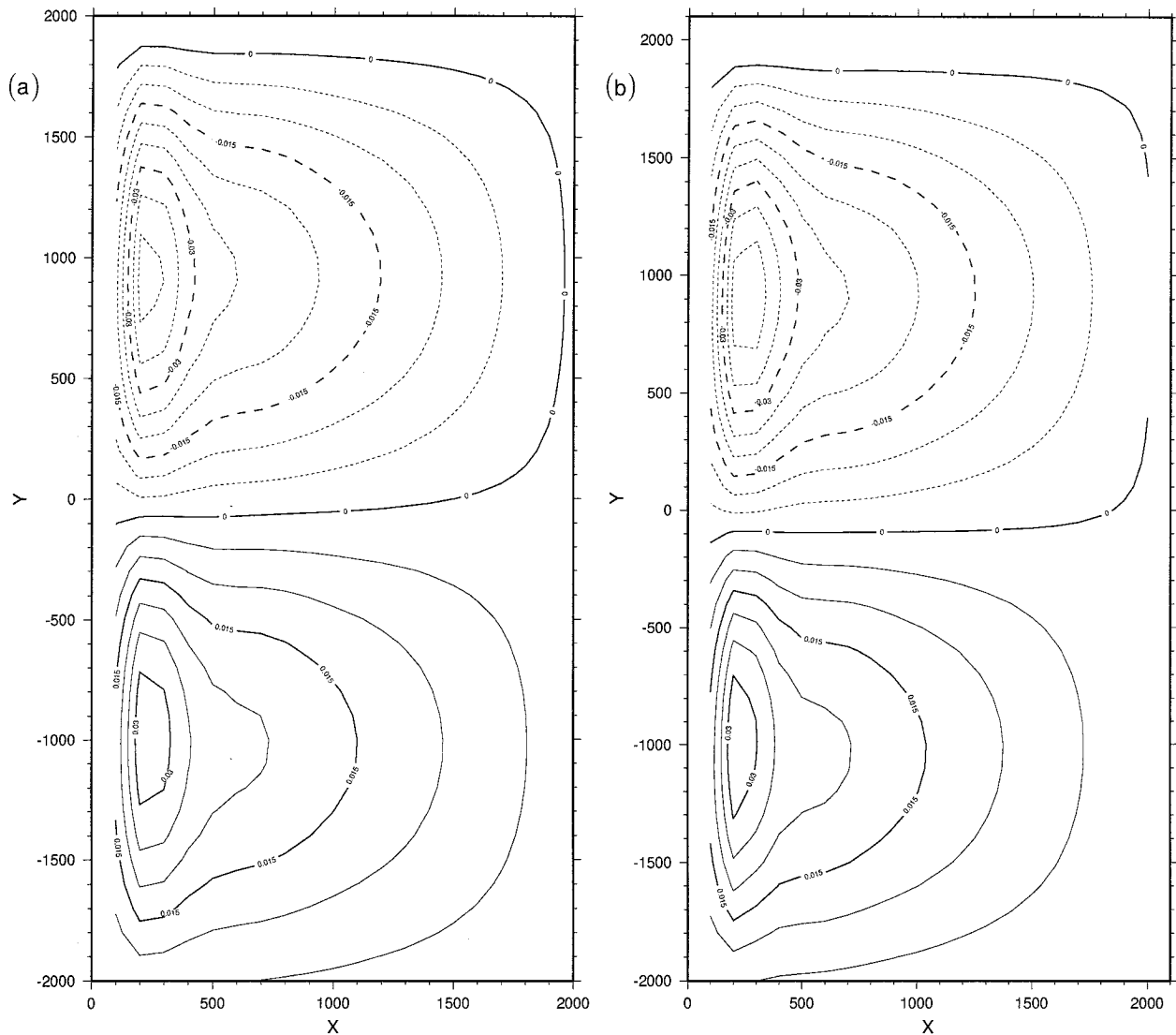
FIG. 13. Barotropic streamfunction Ψ after one year of integration for (a) the flat bottomed β-plane calculation and (b) the *f*-plane calculation with sloping bottom.

formulated using a barotropic streamfunction so that the zonal transport is easily specified for all time. In the finite-volume model, we mimic the boundary conditions on the zonal transport by relaxing the zonal flow toward the initial conditions on a timescale of 1 h in a narrow band upstream of the bump (0 < x < 50 km). This relaxation supplies a force that balances the decelerating form drag exerted by the bump.

The flow in both models is immediately deflected to the left as it passes over the bump. In time, an anticyclonic and cyclonic eddy are formed, the latter of which is shed off the bump and advected downstream (see Figs. 14, 15a).

The effect of the topography in steering the flow is represented in a very similar manner in both models. The distortion of the cyclonic tail, upstream of the

bump in the shaved cell calculations, is a result of the cyclonic eddy impinging on the band of relaxation and should be ignored. The orientation of the elliptic cyclonic eddy is slightly different, but the process of eddy formation, shedding, and advection modeled in SPEM is properly duplicated in the piecewise linear shaved cell calculation. Remember that in addition to their respective coordinates, the models differ in the distribution of resolution, both vertical and horizontal, and the orientation of the surface along which dissipation occurs. The SPEM solution appears smoother than the finite-volume model solution. This might be attributed to the fact that the seamount intersects levels of the finite-volume model, thereby introducing discontinuities, whereas there are no lateral boundaries on a σ surface other than at the channel
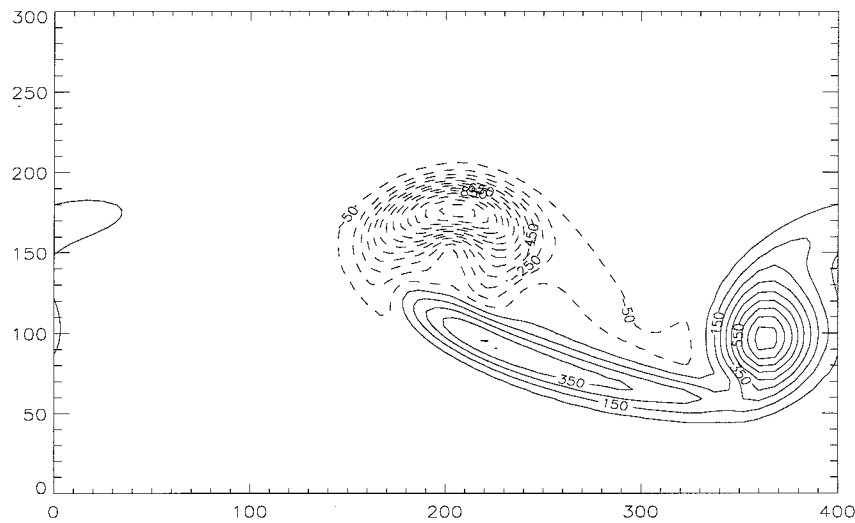
FIG. 14. Nondimensional depth integrated relative vorticity $\hat{\zeta}/f$ in the SPEM integration, at t = 10 days. Contour interval is 100. The features to note are the anticyclonic eddy positioned over the bump (center), the cyclonic eddy swept downstream, and a tail of cyclonic vorticity that stretches between the bump and the downstream eddy.

walls. Despite these differences, it is clear that the shaved cell method does a comparable job to that of the σ-coordinate model in representing flow even over this large topographic feature.

c. Comparison of piecewise linear shaved cells with step topography

In order to assess the merits of our various methods of representing topography using finite volumes, we repeated the above integration using the partial-step and full-step representations with exactly the same parameters. The bump profiles as seen by the model are shown in Fig. 16. The three curves correspond to the three representations used (the solid curve is the profile used in the shaved cell approach). In both stepwise approaches, the profiles are discontinuous but because of the particular resolution generally follow the Gaussian shape. This is because the aspect ratio of the grid cell ($\Delta z/\Delta x$) is comparable with the slope of the topography ($\sim h/L$):

$$\frac{\Delta z}{\Delta x} = \frac{562.5 \text{ m}}{5 \text{ km}} = 0.1125$$

and

$$\frac{h}{L} = \frac{4050 \text{ m}}{25 \text{ km}} = 0.162.$$

The model was initialized and integrated forward as before. Figures 15b and 15c show the depth-integrated relative vorticity normalized by f at day 10. Both step approaches manage to model the process of eddy formation, shedding, and advection. The notable differences between piecewise linear and partial step are (i)

the larger maxima within the tail structure in the partial step and (ii) the tendency in the partial step for the end of the tail above the bump to split in two. On the whole, however, the solutions are qualitatively similar, although the piecewise linear slope solution most resembles the SPEM solution. The differences between the solutions using partial-step and full-step approximations are more significant: (i) stronger local maxima within the tail structure, (ii) a complete split in the end of the tail rendering an isolated cyclonic feature that is almost as strong as the cyclonic eddy itself, (iii) a stronger, wide band of cyclonic vorticity positioned off the northeastern flank of the bump, and (iv) much more small-scale noise over the bump itself.

In this example, the horizontal scale of topographic variation was well resolved; the aspect ratio of the grid cell is near that of the slope. Ironically, as the height of the bump is reduced, more levels would be needed in the "full step" method to "properly" resolve the slope.

All numerical methods should asymptote to the "correct" solution as the resolution becomes finer. To test the convergence properties of the various topographic representations, we conducted two additional experiments for each representation, one with $\Delta x = 3\frac{1}{3}$ km and the second with $\Delta x = 2\frac{1}{2}$ km, keeping the vertical resolution unchanged (i.e., using eight levels). The time step was reduced to $\Delta t = 200$ s and $\Delta t = 100$ s, respectively, but all other parameters remained unchanged. As we increase the *horizontal* resolution (i.e., reduce Δx) one expects the "piecewise linear slope" and "partial step" solutions to converge to the same "correct" solution.

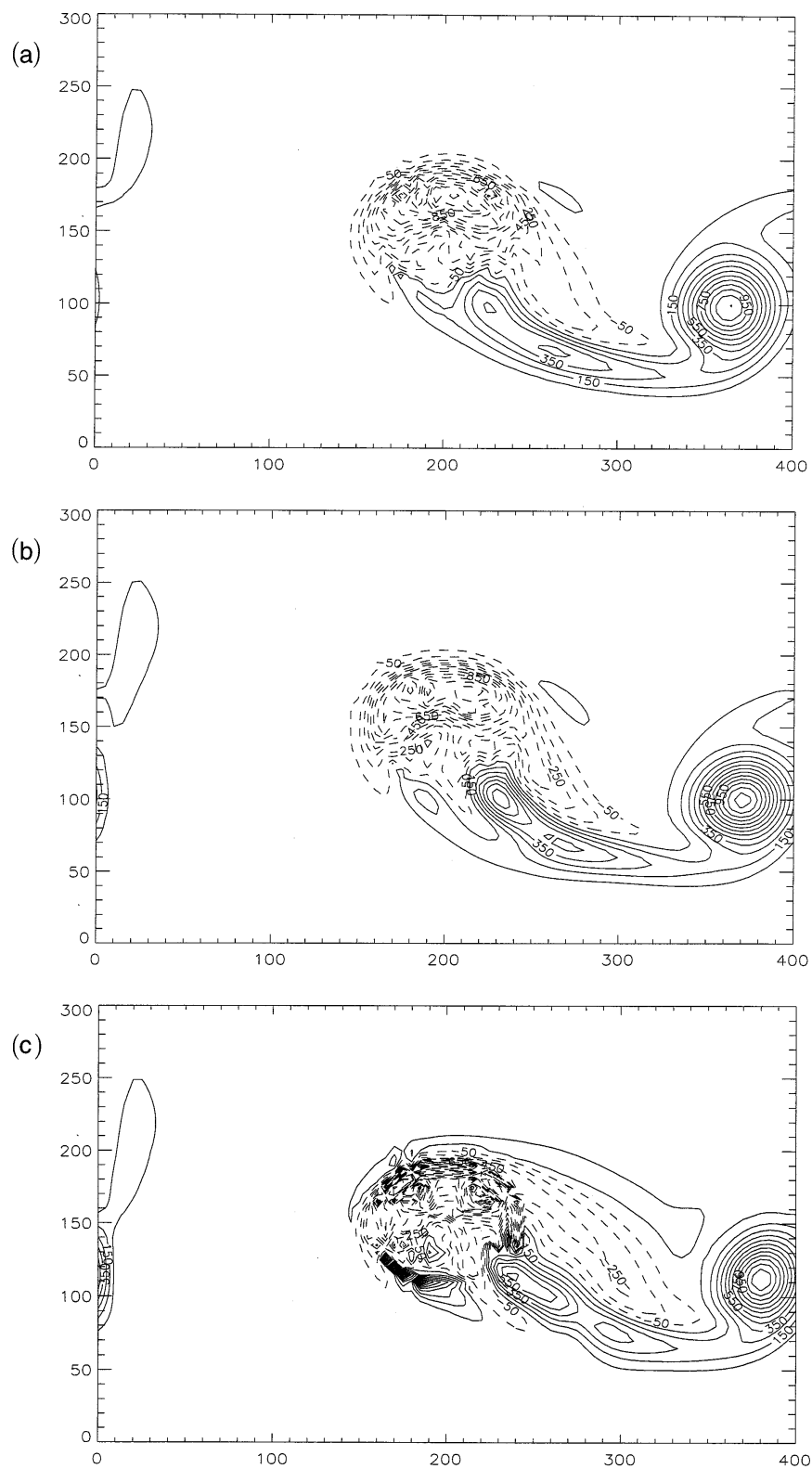Figures 17a and 18a show the "piecewise linear

FIG. 15. Nondimensional depth integrated relative vorticity $\hat{\zeta}/f$ at $t = 10$ days using (a) piecewise linear, (b) partial-step, and (c) full-step representations of topography. Contour interval is 100. The distorted tail of cyclonic vorticity upstream of the bump ($0 < x < 50$ km) is an artifact of the band of relaxation used to mimic open boundaries in a periodic channel.
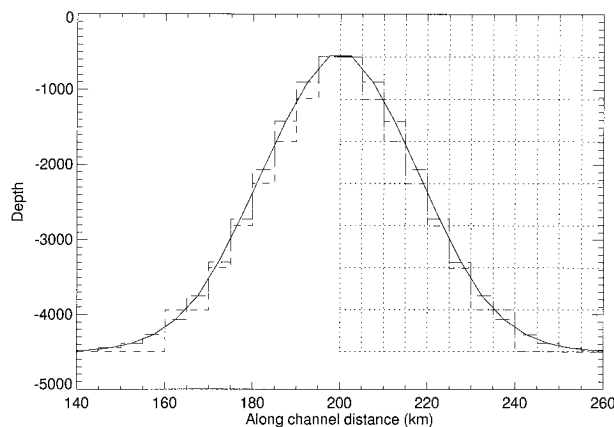
FIG. 16. Profiles of bottom depth in the three shaved cell calculations of zonal flow over a Gaussian bump. The solid line is the piecewise linear representation the nodal points of which fall exactly on the Gaussian curve being modeled. The short-dashed curve and long-dashed curve correspond to the partial-step and full-step representations, respectively. Note that the full-step topography fits the model grid that has been overlaid on the right. To the eye, all curves should look approximately Gaussian, but on closer examination it becomes clear that the full step curve is a poor local approximation to the topography, while the partial step is closer even though it is discontinuous.

slope'' solutions for the two finer resolutions of $\Delta x = 3\frac{1}{3}$ km and $\Delta x = 2\frac{1}{2}$ km, respectively. The solutions differ from the former calculations (Fig. 15a) only in fine detail, the overall structure being the same. The amplitude of the cyclonic eddy reduces as the resolution is made finer, suggesting that coarse resolution overestimates the eddy strength.

The "partial step" solutions, shown in Figs. 17b and 18b, differ more substantially from the low-resolution calculation (Fig. 15b). The tail structure has lost the two tongued feature and becomes even more similar to the "piecewise linear slope" solution. Indeed, the finest resolution "piecewise linear slope" and "partial step" calculations are almost indistinguishable.

In the case of the "full step" method, the solution appears to diverge! Figures 17c and 18c show the solution for $\Delta x = 3\frac{1}{3}$ and $\Delta x = 2\frac{1}{2}$, respectively. Note that as the resolution is increased, the degree of noise above the bump becomes worse, the cyclonic eddy is distorted, and a new anticyclonic eddy appears between the cyclone and the bump. The "rings" of grid-scale noise become more pronounced with increased resolution and clearly delimit the steps of the bump.

We can assess the degree of convergence by comparing the strength of the cyclonic eddy, the values of which are shown in Table 3. As the grid spacing is reduced, the strength of the cyclone reduces but asymptotically so. We have taken the liberty of extrapolating the strengths to the limit of infinite resolution (right-hand column) by using second-order rational functions that pass through the three data points. Based on three experiments each for the three representations, it appears

that the "piecewise linear slope" and "partial step" solutions are converging on the same solution ($\sim 731 \pm 5$), but the "full step" solution appears to be asymptoting to a completely different solution (~ 508). In fact, the full-step method does not approach a sensible solution; in the finest resolution case, there are patches of cyclonic vorticity above the bump (variations at the grid scale) that reach a magnitude twice that of the cyclonic eddy! To explain why the "full step" solution does not converge to the proper solution, in the limit of very high horizontal resolution, we need only point out that the model topography itself does not converge to a Gaussian bump because the vertical resolution is fixed; instead, the topography asymptotes to a stack of seven vertical cylinders. We can only expect the solution to improve if we increase the vertical resolution with the horizontal resolution, thereby allowing the model topography to asymptote to a Gaussian bump.

This series of experiments clearly indicates that the shaved-cell representations (both piecewise linear slope and partial step) converge to a sensible solution with increased horizontal resolution. The "piecewise linear slope" method appears, as expected, to converge with greatest rapidity in that the structure of the solution changes less as the resolution increases and the amplitudes are closer to the asymptotic value. The "full step" method, on the other hand, does fortuitously well at low resolution (because we are modeling a steep topographic slope) but becomes progressively worse as the horizontal resolution is increased. This can be understood in light of the idealized two-dimensional experiments presented earlier that isolated problems associated with "full step" topography.

6. Summary

A finite-volume approach for use in height coordinate ocean models has been outlined, which endows them with a superior treatment of topography. In the interior of the ocean, the scheme reduces to a conventional flux-form finite-difference model. However, "finite volumes" makes possible the use of irregularly shaped volumes that can readily be employed to represent the topography using "shaved cells."

Two idealized experiments were designed to illustrate the advantage of the "shaved cell piecewise linear slope" representation over conventional "full-step topography." In the passive tracer experiment, it was demonstrated that discontinuities in ocean depth that result from the use of step topography led to discontinuities in a steady flow that, in turn, led to noise in the *passive* tracer field. In a similarly configured dynamical model, we show that grid-scale gravity waves are generated by flow over discontinuities inherent in step topography. Within the same conceptual framework, but by shaving the cells with piecewise slopes, these problems are avoided.

The approach set out here, motivated by considera-
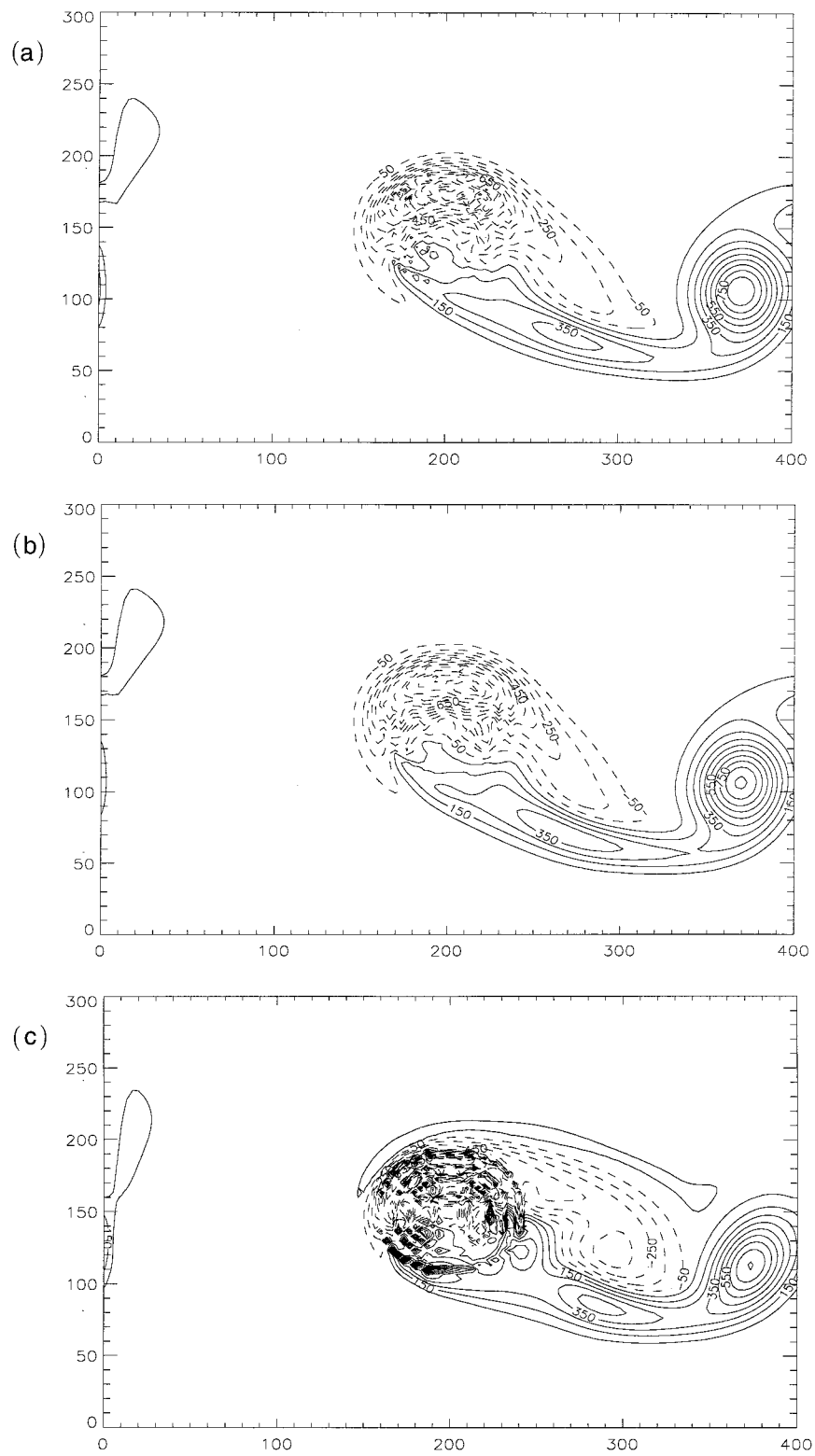
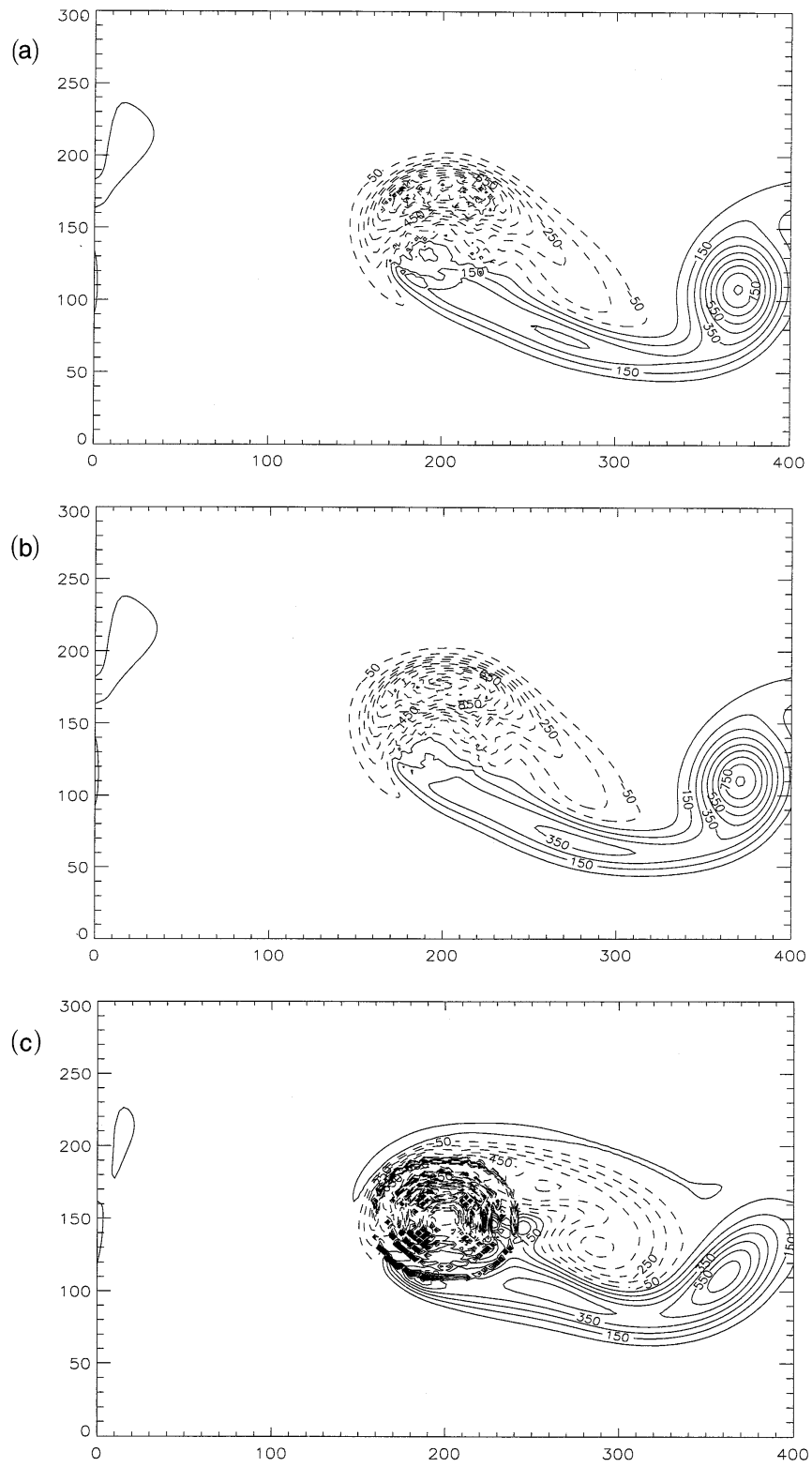FIG. 17. As in Fig. 15 but with horizontal resolution $\Delta x = 3\frac{1}{3}$ km.

FIG. 18. As in Fig. 15 but with horizontal resolution $\Delta x = 2\frac{1}{2}$ km.

TABLE 3. Maximum nondimensional cyclonic vorticity measured in the center of the cyclonic eddy.

Topographic representation	Resolution			Extrapolation $\Delta x \rightarrow 0$
	$\Delta x =$ 5 km	$\Delta x =$ 3⅓ km	$\Delta x =$ 2½ km	
Piecewise linear slope	1152	946	860	736
Partial step	1305	971	861	724
Full step	1234	858	711	508

tions of energy conservation, is fully implemented in the model of Marshall et al. (1997a). Two experiments of oceanic interest were carried out with the model to test the representation of topography. For low–Rossby number flow of a homogeneous ocean, we numerically reproduced the dynamical equivalence of planetary and topographic β. An example in a more nonlinear regime, that of zonal, stratified flow over a Gaussian bump, showed close agreement with a well-established σ-coordinate model, SPEM. However, because we use height as a vertical coordinate we have none of the well-known problems associated with terrain-following coordinate models.

A comparison between piecewise linear slope, partial-step, and the conventional full-step representations clearly indicates that the shaved cell representations are superior. The piecewise linear slope method is the most conducive to smooth, accurate representation, but we note that the partial-step method (as used by Semtner and Mintz 1977) is a good compromise for shallow slopes.

The smoothness of the solutions is a function of the resolution of the topographic variations. That is, if the topography varies substantially on the grid scale, then the dynamical response will be at the grid scale. This means that even using an accurate representation of topography (e.g., piecewise linear or even higher-order representations), steep slopes that cross several model levels in one or few model grid lengths will inevitably appear discontinuous and thus force grid-scale noise.

In the case of shallow slopes (i.e., changes of depth of a grid level or less over horizontal scales of many grid lengths), the shaved-cell approaches, both piecewise linear and partial-step, have clear advantages over the conventional full-step approach. Indeed, the latter is utterly unable to represent the slope and thus cannot be used to model the influence of such topography on the ocean circulation. One might expect that the ocean's high-frequency response to wind forcing, which is largely barotropic, could be poorly modeled with a full-step topography.

We draw an analogy between the various choices of topographic representation and methods for evaluating the area under a curve. In Simpson's method of integration, a series of columns that approximately fit the curve are used. The method converges and is accurate if we use more columns. The trapezoidal method is capable of exactly representing a higher-order function (an inclined line) and subsequently needs fewer columns to achieve the same accuracy. More often than not, higher-order methods are not required because the trapezoidal method is sufficiently accurate with a moderate number of columns. Note that we never consider using a method that is lower order than Simpson's because the curve would be reduced to a series of large steps. Quite unthinkable!

a. Computational overhead

The relative merits of the three representations of topography discussed involve issues other than accuracy and fidelity of representation. There are important practical considerations to be taken into account:

1) cost in terms of arithmetic computation,
2) cost in terms of memory,
3) complexity of code, and
4) accuracy.

It turns out that the number of computations is essentially the same for an optimized finite-difference code as for a general finite-volume code. The general shaved cell code (including piecewise linear slope) requires four parameters for any grid cell that abuts a boundary. In principle, if the topography is never steep, these parameters could be stored in four 2D arrays. This is not possible when the topography intersects more than one level in a single water column, and more sophisticated storage methods then have to be invoked. The simple way forward is to store the parameters for all cells in full 3D arrays, even though the areas and volumes in the interior are constant. However, this does involve a large memory requirement since on a C grid there a four distinct sets of volumes with four parameters each: a tracer volume and three momentum volumes, which introduces a further 16 full 3D arrays, perhaps doubling the memory requirement of a conventional ocean model. On the other hand, the partial step method can be coded using a single 2D array to describe the geometry since, by definition, the topography can only intersect one model level at a time. In this case, the additional memory requirement is nominal but the cell geometries would then have to be calculated as needed, introducing a small computational overhead.

There is no additional code complexity for the general shaved-cell dynamical model; no conditional ("if") statements are needed making the code highly vectorizable. If the memory-saving option of storing the topography in a 2D array is used in the case of partial steps, then the additional code needed to calculate cell geometries would be interspersed with the dynamical code, making the code less transparent to a user.

b. Computational stability

Explicit time integration schemes are generally stable if the grid spacing is greater than the distance that the

fastest waves can travel in a model time step ($\Delta x > c\Delta t$). In the case of tracer advection with shaved cells, the effective grid spacing can be estimated by considering the terms in the x and z directions:

$$\mathcal{V}^\theta \frac{\partial}{\partial t}\theta = -\overline{u\mathcal{A}_x^\theta \delta_x \theta}^x - \overline{w\mathcal{A}_z^\theta \delta_z \theta}^z.$$

The effective grid spacing in x and z directions is approximately

$$\Delta x_{\text{eff}} \sim \frac{\mathcal{V}^\theta}{\overline{\mathcal{A}_x^\theta}^x} \quad \text{and} \quad \Delta z_{\text{eff}} \sim \frac{\mathcal{V}^\theta}{\overline{\mathcal{A}_z^\theta}^z}.$$

For arbitrarily shaved cells, the model can become unstable for a given time step in regions where the effective grid spacing has become too small. To avoid this, we restrict the minimum size that a volume can take by either adding or taking away land from the topography. To some degree, this reverts to the philosophy of step topography, but here the errors are obviously much less since the amount by which we need to change the depth of the ocean is much less, typically less than a few percent.

In the case of partial steps, it turns out that this CFL issue only applies in the vertical direction. Consider a partial cell of depth h. Then the above effective grid spacing becomes

$$\Delta x_{\text{eff}} \sim \Delta x_{\text{regular}} \quad \text{and} \quad \Delta z_{\text{eff}} \sim h.$$

The effective horizontal grid spacing is that of the regular grid. To avoid a restrictive CFL limit to vertical motions, we can again limit the range of h by adding or taking away land from the topography.

c. Arbitrary volumes

We mentioned that the topography could be represented by higher-order polynomials. In three dimensions, such a polynomial could have only seven degrees of freedom since the model has seven attributes per cell (one volume and six areas). The volume and areas might alternatively be found by evaluating the "true" volumes and areas of the ocean from high-resolution datasets without going through the step of fitting curves to the topography. We note that for a given set of volumes and areas, there is no unique topography that corresponds to those volumes and areas. Having generated the volumes and areas, the shape of the topography is therefore open to interpretation.

A higher-order polynomial representation could quite easily be used within each cell; since the (3D) cell has seven degrees of freedom (six areas and one volume), a third-order, 2D polynomial might be used. We have not fully explored higher-order representations since there are many choices to be made about the form of the polynomial. We feel that the piecewise linear slope is sufficiently accurate for most purposes but higher-order representations would be more accurate and could be considered.

d. Less vertical resolution

It is evident from the experiments shown that the piecewise slope representation lessens the need for high vertical resolution to resolve the topography. Lindzen and Fox-Rabinovitz (1989) suggest that the vertical and horizontal resolution of atmospheric models should have the same aspect ratio as the motion. In the ocean, the aspect ratio of the motion under quasigeostrophic scaling goes like $L/H \sim N/f$. High vertical resolution is needed more in the upper ocean since it is much more stratified than at depth. In current height coordinate models, moderately high resolution is needed throughout the water column just to resolve (albeit poorly) the topography. The use of shaved cells means that the vertical resolution can be chosen to better resolve water masses and vertical structure.

e. Coasts

It should be self evident that the piecewise linear slope representation can also be used to shave cells laterally and therefore employed to represent the coasts. In both the partial and full step methods, the coastline assumes a blocklike structure (just like step topography) and would be improved using the piecewise linear slope method that allows the coast to intersect the model cells.

f. General applicability

The finite-volume method bears much similarity with the finite-difference method written in flux form. Since most z-coordinate models are built using this method, the implementation of "shaved" cells ought to be possible. The applicability for use in other coordinate systems has not been investigated. The formal derivation of layer models is based on volume conservation between material surfaces, which is essentially a time-varying finite-volume method. The ability to shave cells is a formal property of the finite-volume formulation, and we anticipate that it is applicable in such models.

APPENDIX A

Discrete Notation

The following notation is used in this paper:

$$\overline{\phi}^x \equiv \frac{1}{2}(u_{i-1/2} + u_{i+1/2})$$

$$\delta_x\phi \equiv u_{i+1/2} - u_{i-1/2}.$$

The interpolation operator, $-x$, is centered and second-order accurate for a regular grid; for irregular grid spacing, errors are first order. This is true also of the discretized differential operator:

$$\frac{\partial}{\partial x}\phi \approx \frac{1}{\Delta x}\delta_x\phi.$$

These operators satisfy the following rules:

$$\delta_\zeta\delta_\eta\phi = \delta_\eta\delta_\zeta\phi \tag{A1}$$

$$\delta_\zeta\overline{\phi}^\eta = \overline{\delta_\zeta\phi}^\eta \tag{A2}$$

$$\overline{\overline{\phi}^\eta}^\zeta = \overline{\overline{\phi}^\zeta}^\eta \tag{A3}$$

$$\delta_\zeta(\phi\psi) = \overline{\phi}^\zeta\delta_\zeta\psi + \overline{\psi}^\zeta\delta_\zeta\phi \tag{A4}$$

$$\delta_\zeta(\overline{\phi}^\zeta\psi) = \phi\delta_\zeta\psi + \overline{\psi\delta_\zeta\phi}^\zeta \tag{A5}$$

$$\overline{\phi\psi}^\zeta = \overline{\phi}^\zeta\overline{\psi}^\zeta + \frac{1}{4}\delta_\zeta\phi\delta_\zeta\psi \tag{A6}$$

$$\overline{\overline{\phi}^\zeta\psi}^\zeta = \phi\overline{\psi}^\zeta + \frac{1}{4}\delta_\zeta(\psi\delta_\zeta\phi), \tag{A7}$$

where ζ and η may be any coordinate. The first three rules (A1)–(A3) are statements of commutivity. Rules (A4) and (A5) are discrete forms of the product rule, $\partial(\phi\psi)/\partial\zeta = \phi\partial\psi/\partial\zeta + \psi\partial\phi/\partial\zeta$. The last two rules, (A6) and (A7), reflect the smoothing effect of the interpolation operator; use of (A7) to express a double interpolation in terms of the central term gives

$$\overline{\overline{\phi}^x}^x = \phi + \frac{1}{4}\delta_x\delta_x\phi \approx \phi + \frac{\Delta x^2}{4}\frac{\partial^2}{\partial x^2}\phi.$$

One unconventional piece of shorthand is

$$\wr\phi\wr_x^2 \equiv \phi_{i-1/2,j,k}\phi_{i+1/2,j,k},$$

which satisfies the rules

$$\wr\phi\wr_\zeta^2 = 2\overline{\overline{\phi}^\zeta\phi}^\zeta - \overline{\phi^2}^\zeta \tag{A8}$$

$$\wr\phi\wr_\zeta^2 = \overline{\phi}^\zeta\overline{\phi}^\zeta - \frac{1}{4}(\delta_\zeta\phi)^2. \tag{A9}$$

This last operator is introduced to keep the notation concise when we consider conservation of second moments in the tracer advection equation. The operator $\wr\phi\wr_\zeta^2$ is the geometric product between two neighboring points.

APPENDIX B

Derivation of Second-Moment Conservation

The discrete advection operator used in (8) is

$$\delta_x(A_x u\overline{\theta}^x) + \delta_y(A_y u\overline{\theta}^y) + \delta_z(A_z u\overline{\theta}^z).$$

Global conservation of the second moment requires that this term multiplied by θ can be written as the divergence of a flux. Considering just the x component, we have

$$\theta\delta_x(A_x u\overline{\theta}^x) = \theta[\overline{A_x u\delta_x\theta}^x + \theta\delta_x(A_x u)]$$

using (A5). The first term on the right-hand side can be written

$$\theta\overline{A_x u\delta_x\theta}^x = \overline{A_x u\overline{\theta}^x\delta_x\theta}^x - \frac{1}{4}\delta_x(A_x u\delta_x\theta\delta_x\theta)$$

$$= \overline{A_x u\delta_x\left(\frac{1}{2}\theta^2\right)}^x - \frac{1}{4}\delta_x[A_x u(\delta_x\theta)^2],$$

where we have used first (A7) and then (A4). Using (A5) again, the first term can then be written

$$\overline{A_x u\delta_x\left(\frac{1}{2}\theta^2\right)}^x = \delta_x\left(A_x u\overline{\frac{1}{2}\theta^2}^x\right) - \frac{1}{2}\theta^2\delta_x[A_x u(\delta_x\theta)^2].$$

Substituting this back into the previous expressions gives

$$\theta\delta_x(A_x u\overline{\theta}^x) = \delta_x\left(A_x u\frac{1}{2}\wr\theta\wr_x^2\right) + \frac{1}{2}\theta^2\delta_x(A_x u),$$

where we have introduced the geometric product operator $\wr\theta\wr_x^2$ using (A9). It then follows that

$$\theta\left[\delta_x(A_x u\overline{\theta}^x) + \delta_y(A_y v\overline{\theta}^y) + \delta_z(A_z w\overline{\theta}^z)\right]$$

$$= \delta_x\left(A_x u\frac{1}{2}\wr\theta\wr_x^2\right) + \delta_y\left(A_y v\frac{1}{2}\wr\theta\wr_y^2\right) + \delta_z\left(A_z w\frac{1}{2}\wr\theta\wr_z^2\right)$$

$$+ \frac{1}{2}\theta^2[\delta_x(A_x u) + \delta_y(A_y v) + \delta_z(A_z w)],$$

which is the equation in section 2b.

REFERENCES

Arakawa, A., and V. R. Lamb, 1977: Computational design of the basic dynamical processes of the UCLA general circulation model. *Methods Comput. Phys.,* **17,** 174–267.

Blumberg, A. F., and H. L. Mellor, 1987: Three-dimensional coastal ocean models. *A Description of a Three-Dimensional Coastal Ocean Circulation Model,* Vol. 4, N. S. Heaps, Ed., American Geophysical Union, 208 pp.

Bryan, K., 1969: A numerical method for the study of the circulation of the World Ocean. *J. Comput. Phys.,* **4,** 347–376.

Cox, M. D., 1977: A numerical ocean model with improved bottom topographic representation. GFDL/NOAA Tech. Rep., 27 pp. [Available from Princeton University, Princeton, New Jersey 08540.]

Haidvogel, D., J. Wilkin, and R. Young, 1991: A semi-spectral prim-

itive equation ocean circulation model using sigma and orthogonal curvilinear coordinates. *J. Comput. Phys.,* **94,** 151–185.

Haney, R. L., 1991: On the pressure gradient force over steep topography in sigma coordinate ocean models. *J. Phys. Oceanogr.,* **21,** 610–619.

Hirsch, C., 1990: *Numerical Computation of Internal and External Flows.* Numerical Methods in Engineering, Wiley & Sons.

Lindzen, R. S., and M. Fox-Rabinovitz, 1989: Consistent vertical and horizontal resolution. *Mon. Wea. Rev.,* **117,** 2575–2583.

Maier-Reimer, E., and U. Mikolajewicz, 1992: The Hamburg large scale geostrophic ocean general circulation model (cycle 1). Tech. Rep. 2, 34 pp. [Available from Deutsches Klima-RechenZentrum, Max-Planck-Institut für Meteorologie, Bundesstraße 55, D-2000 Hamburg 13, Germany.]

Marshall, J., A. Adcroft, C. Hill, L. Perelman, and C. Heisey, 1997a: A finite-volume, incompressible Navier–Stokes model for studies of the ocean on parallel computers. *J. Geophys. Res.,* **102** (C3), 5733–5752.

——, C. Hill, L. Perelman, and A. Adcroft, 1997b: Hydrostatic, quasi-hydrostatic and non-hydrostatic ocean modeling. *J. Geophys. Res.,* **102** (C3), 5753–5766.

Mellor, G. L., T. Ezer, and L.-Y. Oey, 1994: The pressure gradient conundrum of sigma coordinate ocean models. *J. Atmos. Oceanic Technol.,* **11,** 1126–1134.

Semtner, A. J., Jr., and Y. Mintz, 1977: Numerical simulation of the Gulf Stream and mid-ocean eddies. *J. Phys. Oceanogr.,* **7,** 208–230.